SIAM J. APPL. MATH.
Vol. 79, No. 5, pp. 1916–1939

DETECTION OF BACKSCATTERED WAVES FROM A TARGET IN CLUTTER FROM A ROTATING SCATTERER*

MARGARET CHENEY†, LOUIS SCHARF†, POORIA PAKROOH†, ANDREW HOMAN‡, AND MATTHEW FERRARA‡

Abstract. We develop a physics-based mathematical model for the signals received from a fixed radar that interrogates a moving target and a single rotating object located in the same range cell. From this mathematical model, we extract a statistical model, and use this model to develop a detector for a linearly moving target in "clutter" produced by the rotating object. In particular, we exploit the second-order correlation structure of wind-turbine clutter to derive a target detector that uses a multipulse coherence statistic consisting of an incoherent geometric average of coherently computed adaptive coherence scores. The detector compares favorably to a multipulse coherence detector that uses no modeling or estimation of the clutter. Although we focus on the case of rotating wind turbines, the analysis applies to other rotating objects such as propellers. Similar models may be used for acoustic signals.

Key words. radar, detection, clutter, wind turbine

AMS subject classifications. 35L05, 60G35

DOI. 10.1137/19M1240496

1. Introduction.

Wind turbine clutter (WTC) presents a significant challenge to detecting targets in civilian radar systems for weather and air traffic control [30], and military systems for early warning and perimeter defense [29]. Much work has been focused on the *forward problem* of numerically solving Maxwell's equations to estimate the effects of WTC given that everything is known (blade lengths, tilt parameters, materials, etc.) a priori about the wind turbine(s) (see, e.g., [9, 22, 23, 25, 30, 47]). This paper, however, is focused on first developing a mathematical model that includes relevant statistical properties of the target and WTC, and then using this model to solve the *inverse problem* of detecting linearly moving targets in confounding WTC.

Mitigating the clutter from wind turbines is difficult because of their large radar cross section, their rotational motion, and their many large modes of vibration that arise from stochastic forcing by the wind [21, 38, 42].

Today's clutter-mitigation algorithms for radar (such as the Gaussian model adaptive processing algorithm [40]), are effectively Doppler high-pass filters which do not sufficiently eliminate the WTC returns from the received signal without degrading the target signal. A variety of such techniques were examined by Butler and Johnson [3] and others [29]. Based on the results of [3], Jackson and Butler [14] outlined various mitigation strategies, including waveform design and beamforming [28] on receive.

*Received by the editors January 24, 2019; accepted for publication (in revised form) July 12, 2019; published electronically October 3, 2019.
https://doi.org/10.1137/19M1240496
Funding: This work was supported by the Air Force Office of Scientific Research under contracts FA9550-14-C-0053, FA9550-14-1-0185, and FA9550-18-1-0087.
†Mathematics, Colorado State University, Fort Collins, CO 80523-1874 (margaret.cheney@colostate.edu, scharf@colostate.edu, pooria.pakrooh@gmail.com).
‡Matrix Research, Inc., Dayton, OH 45432 (andrew.homan@matrixresearch.com, matthew.ferrara@matrixresearch.com).

Related range-Doppler notching approaches include [8] and [12, 13]. Other approaches include fuzzy-logic detectors [10, 11, 20] and expoitation of sharp changes in the Doppler spectrum [24].

In [26], Naqvi and Ling present results for the (theoretically ideal) model-then-subtract approach to WTC mitigation. In particular, each blade is modeled as a summation of point scatterers in order to adequately simulate the polarimetric response of a wind turbine. The precise amplitudes of the point scatterers are determined on-the-fly using a greedy basis pursuit algorithm, and the model is used to detect a moving target in synthetic WTC data. Uysal et al. [46] also use a sparse signal model for the WTC, but their approach exploits a simpler short-time Fourier transform (STFT) basis, in which sparse STFT coefficients indicate the presence of WTC. Thus although some progress in fielded systems has been made [39], in general the problem remains open.

In this paper, as in [26, 46] and others, we consider a staring radar with both a linearly moving target and clutter from a wind turbine in its field of view. We develop a physics-based mathematical model for the scattering, and then use it to derive a generalized likelihood ratio detector. This detector uses a sequence of adaptive coherence (ACE) scores [18, 19, 34] and geometrically averages them to compute a multipulse coherence statistic. This statistic is called a multipulse adaptive coherence estimator (MPACE), for its close connection to ACE. The detector is firmly grounded in detection theory in the multivariate normal model. Its innovation is its use of incoherent geometric averages of coherent ACE scores, based on target and clutter modeling. MPACE scores may be computed in the time domain or the frequency domain; in this paper we consider only the time-domain model.

We refer the reader to [18] for an account of the provenance for first-order coherence detectors, including ACE and related detectors. This provenance includes the original work of Kelly [15], Kelly and Forsythe [16], Chen and Reed [4], Robey et al., [31], Scharf and Friedlander [35], Conte, Lops, and Ricci [5, 6], Scharf and McWhorter [34], McWhorter, Scharf, and Griffiths [36], Kraut and Scharf [17], Kraut, Scharf, and Butler [19].

The closely related multipulse coherence estimator (MPCE) statistic is derived for multirank signals in [37], using likelihood theory. It was first reported, for the rank-one case, in 2015 by Abramovich and Besson [1], as an approximation to a Bayesian likelihood. So our MPACE, which accommodates multirank signals and uses secondary data to estimate the covariance $\mathbf{R}$, is an adaptive version of MPCE. A fuller account of the connection between MPACE and prior work of [5, 6, 34, 36], and [1] may be found in [37].

Our paper [27], which is closely related to the present one, begins with a simpified statistical model and presents two statistical detectors. This paper, in contrast, focuses on the physical scattering model from which we show how to extract the simplified statistical model of [27]. In the present paper we include a summary of the statistical results, and also include, in the appendix, a more complete mathematical derivation of the detector.

Although our discussion refers to radar scattering from wind turbines, the same analysis may be applied to electromagnetic or acoustic scattering from other rotating objects [2].

2. Mathematical model of scattering. The development of a mathematical model involves a number of components: the model for wave propagation and scattering, the model for the transmitted signal, a model for signal reception, and models for

the moving target and the moving clutter. We consider explicitly the electromagnetics case, but the same results apply equally well to the acoustics case.

2.1. Scalar model for electromagnetic wave propagation. Rather than the full Maxwell's equations, we use the simplified scalar model

$$\left(\nabla^2 - \frac{1}{c^2}\frac{\partial^2}{\partial t^2}\right)\mathcal{E}(t,\boldsymbol{x}) = j(t,\boldsymbol{x}), \tag{2.1}$$

where $\mathcal{E}(t,\boldsymbol{x})$ denotes one Cartesian component of the electric field, j is proportional to one Cartesian component of the time derivative of the current density on the source (antenna or scattering object), and where c is the speed of light in dry air, which we take to be the same as vacuum.

2.2. The Green's function. To obtain a useful approximation to solutions of (2.1), we make use of the outgoing Green's function [7, 44, 48]

$$g(t,\boldsymbol{x}) = \frac{\delta(t-|\boldsymbol{x}|/c)}{4\pi|\boldsymbol{x}|} \tag{2.2}$$

which satisfies the equation

$$\left(\nabla^2 - \frac{1}{c^2}\frac{\partial^2}{\partial t^2}\right)g(t,\boldsymbol{x}) = -\delta(t)\delta(\boldsymbol{x}). \tag{2.3}$$

Here $|\boldsymbol{x}|$ denotes the length of the vector $\boldsymbol{x}$. Convolution by the Green's function can be thought of as an operation that propagates the field from one space-time point to a different space-time point.

2.3. The field incident upon scatterers. The field $\mathcal{E}^{\text{in}}$ emanating from the antenna is obtained by solving (2.1) when the source j corresponds to the current density on the antenna. For now, we use a simplified pointlike antenna model, for which $j(t,\boldsymbol{x}) = s(t)\delta(\boldsymbol{x}-\boldsymbol{x}^0)$, where s is the waveform transmitted by the antenna. The field incident upon the scatterers is then

$$\mathcal{E}^{in}(t,\boldsymbol{x}) = \int g(t-t',\boldsymbol{x}-\boldsymbol{x}^0)s(t')dt' = \frac{s(t-|\boldsymbol{x}-\boldsymbol{x}^0|/c)}{4\pi|\boldsymbol{x}-\boldsymbol{x}^0|}. \tag{2.4}$$

For a pulsed radar, the source waveform is of the form

$$s(t) = \sum_{p}^{P-1} u(t-pT), \tag{2.5}$$

where T is the pulse repetition interval. The pulse $u(t)$ typically has compact support $(0,t_0]$, where $t_0 < T$. This introduces a separation of time scales: the wave propagates on the "fast time" scale t, whereas objects typically move on the "slow time" scale pT.

2.4. Simplified scattering model. All of our analysis below assumes additive, first-order scattering from wind turbine scattering centers. This assumption neglects any multiple scattering.

In particular, we use the single-scattering (Born) approximation [32, 41], in which we assume that the field $\mathcal{E}^{\text{in}}$ radiated by the antenna produces, on the scatterer, a secondary source that is proportional to the incident field $\mathcal{E}^{\text{in}}$. The proportionality

"constant" we denote by $V(t,\boldsymbol{x})$, which we call the reflectivity function. In other words, in (2.1), we take $j(t,\boldsymbol{x}) = V(t,\boldsymbol{x})\mathcal{E}^{\text{in}}(t,\boldsymbol{x})$. Thus the field received back at the antenna is assumed to be

$$\mathcal{E}^{\text{sc}}(t,\boldsymbol{x}) \approx \mathcal{E}_B(t,\boldsymbol{x}) := \iint g(t-\tau,\boldsymbol{x}-\boldsymbol{z})V(\tau,\boldsymbol{z})\mathcal{E}^{\text{in}}(\tau,\boldsymbol{z})d\tau d\boldsymbol{z}. \tag{2.6}$$

This is simply a convolution of the space-time Green's function with the (Born-approximated) induced current density.

2.5. Model for the scattered field. With (2.4), the Born-approximated scattered field (2.6) back at the antenna location $\boldsymbol{x}^0$ is

$$\begin{aligned}\mathcal{E}_B^{sc}(t,\boldsymbol{x}^0) &= \int g(t-\tau,\boldsymbol{x}^0-\boldsymbol{y})V(\tau,\boldsymbol{y})\frac{s(\tau-|\boldsymbol{x}^0-\boldsymbol{y}|/c)}{4\pi|\boldsymbol{x}^0-\boldsymbol{y}|}d\tau d\boldsymbol{y}\\ &= \int \frac{V(t-|\boldsymbol{x}^0-\boldsymbol{y}|/c,\boldsymbol{y})}{(4\pi|\boldsymbol{x}^0-\boldsymbol{y}|)^2}\, s\big(t-2|\boldsymbol{x}^0-\boldsymbol{y}|/c\big)\, d\boldsymbol{y}.\end{aligned} \tag{2.7}$$

For waveforms of the form (2.5), and with scattering objects not too distant from the antenna, we make the start-stop approximation, which assumes that the scattering objects do not move significantly during the transit time of the pulse. The field scattered from the pth pulse is then approximately

$$\mathcal{E}_p^{sc}(t-pT) \propto \int \frac{V(pT,\boldsymbol{y})}{(4\pi|\boldsymbol{x}^0-\boldsymbol{y}|)^2}\, u\big(t-pT-2|\boldsymbol{x}^0-\boldsymbol{y}|/c\big)\, d\boldsymbol{y} \qquad \text{for } pT < t \le (p+1)T. \tag{2.8}$$

We have also noted that the right side depends only on the pulse number p and the time $t-pT$ that has elapsed since the start of the pth pulse, and we have reflected this in the notation on the left side. On the left side we have also dropped the position $\boldsymbol{x}^0$, which remains fixed throughout, and since the Born approximation is used throughout, we have replaced the subscript B by the subscript p to indicate that this is the signal from the pth transmitted pulse.

In (2.8), we shift the origin of time to the start of the pth pulse (i.e., write $t' = t-pT$) to obtain

$$\mathcal{E}_p^{sc}(t') \propto \int \frac{V(pT,\boldsymbol{y})}{(4\pi|\boldsymbol{x}^0-\boldsymbol{y}|)^2} u\left(t'-2|\boldsymbol{x}^0-\boldsymbol{y}|/c\right) d\boldsymbol{y} \tag{2.9}$$

for $0 < t' \le T$.

Equation (2.9) shows the action of the scattering system on the transmitted pulse u. The waveform undergoes a round-trip travel-time delay of $2|\boldsymbol{x}^0-\boldsymbol{y}|/c$ and is attenuated, first by a factor of $4\pi|\boldsymbol{x}^0-\boldsymbol{y}|$ as it spreads out from the source, and then by a second factor of $4\pi|\boldsymbol{x}^0-\boldsymbol{y}|$ as it spreads out after it scatters from the target component at location $\boldsymbol{y}$.

3. Radar signal processing.

3.1. Narrowband waveforms. Most radar systems use transmitted waveforms u that are narrowband, which is to say, $u(t) = \text{Re}\{w(t)e^{i\omega_c t}\}$, where the Fourier transform of $w(t)$ is supported in a narrow band around the origin. In this case, the corresponding scattered field (2.8) becomes

$$\mathcal{E}_p^{sc}(t') \propto \int \frac{V(pT,\boldsymbol{y})}{(4\pi|\boldsymbol{x}^0-\boldsymbol{y}|)^2}\text{Re}\left[w\left(t'-2|\boldsymbol{x}^0-\boldsymbol{y}|/c\right)e^{i\omega_c(t'-2|\boldsymbol{x}^0-\boldsymbol{y}|/c)}\right] d\boldsymbol{y}. \tag{3.1}$$

After demodulation, the baseband complex signal is

$$z_p(t') \propto \int \frac{V(pT,\boldsymbol{y})}{(4\pi|\boldsymbol{x}^0-\boldsymbol{y}|)^2} w\left(t'-2|\boldsymbol{x}^0-\boldsymbol{y}|/c\right) e^{-2i\omega_c|\boldsymbol{x}^0-\boldsymbol{y}|/c} d\boldsymbol{y}. \tag{3.2}$$

3.2. Matched filtering. To improve the ratio of signal energy to noise power, the radar system typically then time shifts the received signal with an hypothesized time delay and correlates the shifted signal with the complex conjugate of the transmitted baseband signal w. This is equivalent to *matched filtering* by convolving the received signal $z_p(t)$ with the time reversal of the complex conjuagate, $\tilde{w}(t) = w^*(-t)$ via

$$d_p(\tau) = \int w^*(t) z_p(t+\tau) dt = \int \tilde{w}(t) z_p(\tau - t) dt \doteq (\tilde{w} * z_p)(\tau). \tag{3.3}$$

When evaluated, this matched filtering produces the output

$$\begin{aligned} d_p(\tau) &= \int w^*(t) \int \frac{V(pT,\boldsymbol{y})}{(4\pi|\boldsymbol{x}^0-\boldsymbol{y}|)^2} w\left(t+\tau-2|\boldsymbol{y}-\boldsymbol{x}^0|/c\right) e^{-2i\omega_c|\boldsymbol{y}-\boldsymbol{x}^0|/c} d\boldsymbol{y} dt \\ &= \int \frac{V(pT,\boldsymbol{y})}{(4\pi|\boldsymbol{x}^0-\boldsymbol{y}|)^2} e^{-2i\omega_c|\boldsymbol{y}-\boldsymbol{x}^0|/c} \underbrace{\int w^*(t) w\left(t+\tau-2|\boldsymbol{y}-\boldsymbol{x}^0|/c\right) dt}_{A(\tau-2|\boldsymbol{y}-\boldsymbol{x}^0|/c)} d\boldsymbol{y}, \end{aligned} \tag{3.4}$$

where

$$A(\tau) = \int w^*(t) w(t+\tau) dt = \int \tilde{w}(t) w(\tau - t) dt \tag{3.5}$$

is the autocorrelation function of w and where the superscript $*$ denotes complex conjugation. The support of A is twice as wide as that of w.

3.3. The far-field approximation. We assume that the radar beam is narrow, so that the region illuminated by the beam within a single range bin (i.e., at a particular value of τ) is small relative to the distance from this region to the radar. Within this region, we choose a particular point, which we take to be the origin. Points $\boldsymbol{y}$ within this region then satisfy the inequality $|\boldsymbol{y}| \ll |\boldsymbol{x}^0|$. Under this condition, we can use the far-field or small-scene approximation

$$\begin{aligned} |\boldsymbol{y}-\boldsymbol{x}^0| &= \sqrt{|\boldsymbol{x}^0|^2 - 2\boldsymbol{x}^0\cdot\boldsymbol{y} + |\boldsymbol{y}|^2} = |\boldsymbol{x}^0|\sqrt{1 - 2\frac{\hat{\boldsymbol{x}}^0\cdot\boldsymbol{y}}{|\boldsymbol{x}^0|} + \frac{|\boldsymbol{y}|^2}{|\boldsymbol{x}^0|^2}} \\ &= |\boldsymbol{x}^0|\left(1 - \frac{\hat{\boldsymbol{x}}^0\cdot\boldsymbol{y}}{|\boldsymbol{x}^0|} + O\left(\frac{|\boldsymbol{y}|^2}{|\boldsymbol{x}^0|^2}\right)\right) = |\boldsymbol{x}^0| - \hat{\boldsymbol{x}}^0\cdot\boldsymbol{y} + O\left(\frac{|\boldsymbol{y}|^2}{|\boldsymbol{x}^0|}\right), \end{aligned} \tag{3.6}$$

where we have used the Taylor expansion $\sqrt{1+a} = 1 + a/2 + O(a^2)$ and where we have written $\hat{\boldsymbol{x}} = \boldsymbol{x}/|\boldsymbol{x}|$. Under the approximation (3.6), (3.4) becomes

$$d_p(\tau) \approx \int \frac{V(pT,\boldsymbol{y})}{(4\pi|\boldsymbol{x}^0|)^2} e^{-2i\omega_c(|\boldsymbol{x}^0|-\hat{\boldsymbol{x}}^0\cdot\boldsymbol{y})/c} A(\tau - 2(|\boldsymbol{x}^0| - \hat{\boldsymbol{x}}^0\cdot\boldsymbol{y})/c) d\boldsymbol{y} \tag{3.7}$$

for $0 < \tau \le T$.

3.4. Radar signal in a single range bin. At the range bin $\tau = 2|\boldsymbol{x}^0|/c$, (3.7) is

$$d[p] \doteq d_p\left(\frac{2|\boldsymbol{x}^0|}{c}\right) \propto \int V(pT, \boldsymbol{y}) e^{2i\omega_c \hat{\boldsymbol{x}}^0 \cdot \boldsymbol{y}/c} A(2\hat{\boldsymbol{x}}^0 \cdot \boldsymbol{y}/c) d\boldsymbol{y}, \tag{3.8}$$

where the argument $\tau = 2|\boldsymbol{x}^0|/c$ is understood on the left side and where on the right we have used the fact that $\exp(-2i\omega_c|\boldsymbol{x}^0|/c)$ and $(4\pi|\boldsymbol{x}^0|)^2$ are constant over this range bin. Below we write $k_c = \omega_c/c$. There should be no confusion between the notations $d_p(\tau)$ and $d[p]$: the former is the output, at time delay τ, of the matched filter due to pulse p, and the latter is the pth such output, evaluated at delay $\tau = 2|\boldsymbol{x}^0|/c$.

4. Model for radar returns from different targets. We now consider two different types of scattering objects V that are undergoing different types of motion. Our strategy is to exploit differences in the motion to distinguish between radar signals coming from the different types of target. We consider first the case of a target moving at constant velocity.

4.1. Linearly moving and vibrating target. We model the reflectivity function for a vibrating, linearly translating target (such as an airplane) as

$$V(t, \boldsymbol{x}) = X(\boldsymbol{x} - \boldsymbol{v}t + \mathcal{T}(t, \boldsymbol{x} - \boldsymbol{v}t)), \tag{4.1}$$

where X denotes the reflectivity function of the target in its own reference frame (say $V(0, \boldsymbol{x}) = X(\boldsymbol{x})$). The vector $\boldsymbol{v}$ denotes target velocity and $\mathcal{T}$ denotes a small[1] displacement due to flexing and vibration. We assume that these vibrations are slow compared with the speed of light; consequently during the pth pulse, we replace the translation $\mathcal{T}(t, \boldsymbol{x} - \boldsymbol{v}t)$ by $\mathcal{T}(pT, \boldsymbol{x} - \boldsymbol{v}pT)$.

At the range bin $\tau = 2|\boldsymbol{x}^0|/c$, (3.8) is

$$d^X[p] \propto \int X\left(\boldsymbol{y} - \boldsymbol{v}pT + \mathcal{T}(pT, \boldsymbol{y} - \boldsymbol{v}pT)\right) e^{2ik_c \hat{\boldsymbol{x}}^0 \cdot \boldsymbol{y}} A(2\hat{\boldsymbol{x}}^0 \cdot \boldsymbol{y}/c) d\boldsymbol{y}, \tag{4.2}$$

where we have written $k_c = \omega_c/c$.

4.1.1. Features of (4.2). The expression (4.2) can be better understood by first transforming to a frame of reference in which the vibrating target is no longer translating, by making the change of variables $\boldsymbol{z} = \boldsymbol{y} - \boldsymbol{v}pT$. This converts (4.2) into

$$\begin{aligned} d^X[p] &\propto \int X\left(\boldsymbol{z} + \mathcal{T}(pT, \boldsymbol{z})\right) e^{2ik_c \hat{\boldsymbol{x}}^0 \cdot [\boldsymbol{z} + \boldsymbol{v}pT]} A(2\hat{\boldsymbol{x}}^0 \cdot (\boldsymbol{z} + \boldsymbol{v}pT)/c) d\boldsymbol{z} \\ &\propto \underbrace{e^{2ik_c \hat{\boldsymbol{x}}^0 \cdot \boldsymbol{v}pT}}_{\text{Doppler}} \int X\left(\boldsymbol{z} + \mathcal{T}(pT, \boldsymbol{z})\right) e^{2ik_c \hat{\boldsymbol{x}}^0 \cdot \boldsymbol{z}} A(2\hat{\boldsymbol{x}}^0 \cdot (\boldsymbol{z} + \boldsymbol{v}pT))/c) d\boldsymbol{z}. \end{aligned} \tag{4.3}$$

At each p, we then change to a frame in which the target is not vibrating with the change of variables $\boldsymbol{z} \mapsto \boldsymbol{z}' = \boldsymbol{z} + \mathcal{T}(pT, \boldsymbol{z})$. This change of variables can be inverted

[1] Intrapulse translation due to vibrations are small enough for the start-stop approximation to be valid: for example, an experimental study of wind turbine vibration modes [21] determined that the dominant vibrations of a wind turbine occur at frequencies less than 10 Hz. Using an absolute worst-case excursion of 77 ft (using the Vestas Model 47 blade length), this results in an off-rotation velocity of 77 ft/.1 sec = 235 m/sec. Using the experiment's 1 μ sec. pulse duration and 11 cm wavelength, the mismodeled range migration is bounded by .235 mm, or approximately wavelength/468, which we consider negligible.

as $\boldsymbol{z} = \boldsymbol{z}' + \tilde{\mathcal{T}}(pT, \boldsymbol{z}')$, where again $\tilde{\mathcal{T}}$ is small.[2] This converts (4.3) to

$$d^X[p] \propto \underbrace{e^{2ik_c\hat{\boldsymbol{x}}^0\cdot\boldsymbol{v}pT}}_{e^{i\theta^X[p]}} \int \underbrace{X(\boldsymbol{z}')\, e^{2ik_c\hat{\boldsymbol{x}}^0\cdot(\boldsymbol{z}'+\tilde{\mathcal{T}}(pT,\boldsymbol{z}'))}}_{q_p^X(\boldsymbol{z}')} A(2\hat{\boldsymbol{x}}^0\cdot[\boldsymbol{z}' + \boldsymbol{v}pT + \tilde{\mathcal{T}}(pT,\boldsymbol{z}')]/c)d\boldsymbol{z}', \tag{4.4}$$

where $\theta^X[p] = p\Theta$ with $\Theta = 2k_c vT$ and $v = \widehat{\boldsymbol{x}}^0 \cdot \boldsymbol{v}$, and where q_p^X is the complex reflectivity

$$q_p^X(\boldsymbol{z}) = X(\boldsymbol{z})\, e^{2ik_c\hat{\boldsymbol{x}}^0\cdot(\boldsymbol{z}+\tilde{\mathcal{T}}(pT,\boldsymbol{z}))} \tag{4.5}$$

with random phase $2k_c\hat{\boldsymbol{x}}^0 \cdot \tilde{\mathcal{T}}(pT, \boldsymbol{z})$.

In (4.4), the complex exponential labeled $e^{i\theta^X[p]}$ has a phase that depends on the velocity; this gives a pulse-to-pulse Doppler shift corresponding to the target motion. We note that this phase is deterministic and depends linearly on the pulse number p. Consequently (4.4) can be written

$$d^X[p] = e^{i\theta^X[p]}\beta^X[p], \tag{4.6}$$

where $\theta^X[p] = p\Theta$ and where $\beta^X[p]$ denotes the integral factor of (4.4). This integral factor represents the overall target reflectivity at pulse p.

The overall target reflectivity $\beta^X[p]$ can be better understood if we assume the support of the scattering function X is smaller than the range resolution of the transmitted waveform. Thus in the integral of (4.4), the ambiguity function A is constant. Consequently $\beta^X[p]$ has the form

$$\beta^X[p] = \int q_p^X(\boldsymbol{z})d\boldsymbol{z}. \tag{4.7}$$

The fact that in (4.7) the contributions from the random phases $2k_c\hat{\boldsymbol{x}}^0 \cdot \tilde{\mathcal{T}}(pT, \boldsymbol{z})$ are integrated over the target leads to the phenomenon known as *scintillation*, in which small relative phase changes cause the overall target reflectivity $\beta^X[p]$ to vary dramatically. The random displacements $\mathcal{T}$, however, are slowly varying. Consequently, we assume that the overall target reflectivity $\beta^X[p]$ is constant over a short sequence of R pulses.

This target model is a Swerling-I target model over a train of R pulses, except that we are treating the target scattering function as a deterministic constant, rather than assigning an exponential density to it, as Swerling did. This and related Swerling models have been the basis for target modeling at least since Swerling's 1954 report [43]. The number R, which is the number of pulses over which the Swerling-I target model holds, could vary depending on the particular target and its velocity. In the theory developed below, R is a tunable design parameter that can be matched to the data.

[2]The inverse function theorem guarantees that the mapping $\boldsymbol{z} \mapsto \boldsymbol{z}' = f(\boldsymbol{z})$ can be inverted provided that $0 \neq \nabla f = \widehat{\boldsymbol{z}} + \nabla_{\boldsymbol{z}}\mathcal{T}$, and the inverse can be written $f^{-1}(\boldsymbol{z}') = \boldsymbol{z}' + \left[f^{-1}(\boldsymbol{z}') - \boldsymbol{z}'\right]$ with the term in square brackets being called $\tilde{\mathcal{T}}$. That $\tilde{\mathcal{T}}$ is small can be seen from the inversion relation $\boldsymbol{z}' = f\left(f^{-1}(\boldsymbol{z}')\right) = \boldsymbol{z}' + \tilde{\mathcal{T}}(pT, \boldsymbol{z}') + \mathcal{T}(pT, \boldsymbol{z}' + \tilde{\mathcal{T}}(pT, \boldsymbol{z}'))$ and the fact that $\mathcal{T}$ is small.

4.1.2. STFT for target. Time-frequency plots are often used in the analysis of moving targets. Below we show how to predict the appearance of the moving target in the STFT plot. This analysis also allows us to determine the velocity resolution obtainable from the use of R pulses over which the target phase is assume to be unchanging.

To this end, we use the discrete Fourier transform on the sequence of R pulses $d^X[p] \approx e^{ip\Theta}\beta^X[m], p = m, m+1, \ldots, m+R-1$ as follows:

$$D_m(e^{i\theta}) = \sum_{p=m}^{m+R-1} d^X[p]e^{-ip\theta} = \sum_{p=m}^{m+R-1} \left(e^{ip\Theta}\beta^X[m]\right) e^{-ip\theta}$$

$$\propto \beta^X[m]\; e^{-i(\theta-\Theta)(R-1)/2} \frac{\sin[(\theta-\Theta)R/2]}{\sin[(\theta-\Theta)/2]}. \tag{4.8}$$

We see that the R-pulse discrete Fourier transform (4.8) is a product of a function of m and a function of θ. Consequently, the target appears in the time-frequency plot ($|D|$ as a color on the m-θ plane with m on the horizontal axis) as a horizontal structure; for large R it appears as a horizontal line. Moreover, the last factor of (4.8) has a maximum at $\theta = \Theta$, and its first zero crossing is at $\theta - \Theta = \pi/R$. The resolution of this method of inferring Θ corresponds to the full width of the main lobe of $\sin[(\theta-\Theta)R/2]$, and the Rayleigh limit to resolution is consequently said to be $2\pi/R$. Because $\Theta = 2k_c vT$, resolution in Θ of $2\pi/R$ corresponds to a resolution in down-range velocity of

$$v = \frac{2\pi}{R}\frac{1}{2k_cT} = \frac{\lambda_c}{2RT}, \tag{4.9}$$

where $\lambda_c = 2\pi/k_c$ is the wavelength of the carrier frequency of the transmitted waveform, T is the duration of the pulse u, and R is the number of pulses over which the phases of the sequence $\{d^X[p]\}_0^{R-1}$ may be assumed to increase linearly with pulse number p. For a typical S-band radar operating at 2.4 GHz, $T = 10^{-3}$ sec, $c = 3 \times 10^8$m/sec, $R = 20$, this amounts to a velocity resolution on the order of 2 m/sec.[3]

4.2. Rotating and vibrating scatterer. We model the reflectivity function for a rotating and vibrating object (such as a blade of a wind turbine) as

$$V(t, \boldsymbol{x}) = B\left(\mathcal{O}_t[\boldsymbol{x} + \mathcal{T}(t, \boldsymbol{x})]\right), \tag{4.10}$$

where B denotes the object's reflectivity in its own reference frame (say $V(0, \boldsymbol{x}) = B(\boldsymbol{x})$). The matrix $\mathcal{O}_t$ denotes an orthogonal matrix at time t, and $\mathcal{T}$ again denotes a small translation due to wind-induced flexing and vibration. (This translation in general is different from the translation for the linearly moving target.) Here we have taken the origin to be located at the center of rotation.

Using (4.10) in (3.8) results in

$$d^B[p] \propto \int B\left(\mathcal{O}_{pT}[\boldsymbol{y} + \mathcal{T}(pT, \boldsymbol{y})]\right) e^{2ik_c\hat{\boldsymbol{x}}^0\cdot\boldsymbol{y}} A(2\hat{\boldsymbol{x}}^0\cdot\boldsymbol{y}/c)d\boldsymbol{y}. \tag{4.11}$$

The model (4.11), in the no-vibration case $\mathcal{T} = 0$, reduces to models of the type that have previously been studied, for example, in [26].

[3] $\frac{2\text{ m}}{\text{sec}} \times \frac{60\text{ sec}}{\text{min}} \times \frac{60\text{ min}}{\text{hr}} \times \frac{1\text{ mile}}{1600\text{ m}} \approx 4.5$ miles/hr.

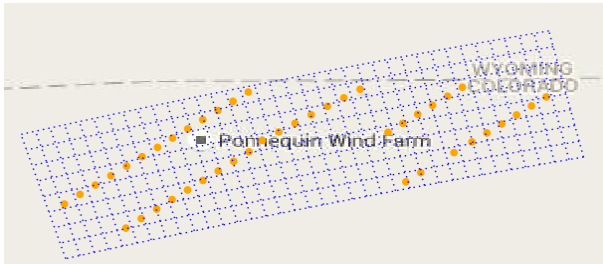

FIG. 1. *A nominal map of the Ponnequin wind farm, near the Colorado–Wyoming border, with orange markers showing the turbine locations. The dotted blue lines are iso-range curves with* $.1^\circ$ *beam demarcations. The beam width for the S-band radar data that we are using is* 1°. *The radar views the wind farm from the bottom right. Map data from Google.*

4.2.1. Example. For the Vestas wind turbines at the Ponnequin wind farm (diagram shown in Figure 1) in southern Wyoming, V is the reflectivity of a 3-bladed rotating target. For the Vestas turbines, the rotation rate is 29 revolutions per minute, or approximately one revolution every 2 seconds. Since the set of rotating blades has 3-fold symmetry, it is invariant under rotation by $2\pi/3$ and, consequently, $B(\boldsymbol{z}) = B(\mathcal{O}(2\pi/3)\boldsymbol{z})$, where $\mathcal{O}(2\pi/3)$ denotes the orthogonal matrix corresponding to rotation by $2\pi/3$.

4.2.2. Interpretation of (4.11). We can understand (4.11) by making the change of variables

$$\boldsymbol{y} \mapsto \boldsymbol{z} = \mathcal{O}_{pT}[\boldsymbol{y} + \mathcal{T}(pT, \boldsymbol{y})], \tag{4.12}$$

which can be approximately inverted as

$$\boldsymbol{y} = \mathcal{O}_{pT}^{-1}(\boldsymbol{z}) - \mathcal{T}(pT, \mathcal{O}_{pT}^{-1}\boldsymbol{z}), \tag{4.13}$$

where we have used the fact that $\mathcal{T}$ is small to approximate $\mathcal{T}(pT, \boldsymbol{y})$ by $\mathcal{T}(pT, \mathcal{O}_{pT}^{-1}\boldsymbol{z})$. This converts (4.11) into

$$\begin{aligned} d^B[p] &= \int B(\boldsymbol{z})\, e^{2ik_c\hat{\boldsymbol{x}}^0\cdot[\mathcal{O}_{pT}^{-1}\boldsymbol{z} - \mathcal{T}(pT,\mathcal{O}_{pT}^{-1}\boldsymbol{z})]} A(2\hat{\boldsymbol{x}}^0 \cdot (\mathcal{O}_{pT}^{-1}\boldsymbol{z} - \mathcal{T}(pT, \mathcal{O}_{pT}^{-1}\boldsymbol{z}))/c)d\boldsymbol{z} \\ &\propto \int \underbrace{B(\boldsymbol{z})\, e^{2ik_c\mathcal{T}(pT,\mathcal{O}_{pT}^{-1}\boldsymbol{z})}}_{q_{pT}^B(\boldsymbol{z})} \underbrace{e^{2ik_c\hat{\boldsymbol{x}}^0\cdot\mathcal{O}_{pT}^{-1}\boldsymbol{z}}}_{\text{Doppler}} A(2\hat{\boldsymbol{x}}^0 \cdot (\mathcal{O}_{pT}^{-1}\boldsymbol{z} - \mathcal{T}(pT, \mathcal{O}_{pT}^{-1}\boldsymbol{z}))/c)d\boldsymbol{z}, \end{aligned} \tag{4.14}$$

where the Jacobian is one because $\mathcal{O}$ is orthogonal, and where q_p is the effective random complex reflectivity

$$q_{pT}^B(\boldsymbol{z}) = B(\boldsymbol{z})\, e^{2ik_c\mathcal{T}(pT,\mathcal{O}_{pT}^{-1}\boldsymbol{z})}. \tag{4.15}$$

In (4.14), the complex exponential labeled "Doppler" has a phase that depends on how the point $\boldsymbol{z}$ rotates with pulse number p; this gives a pulse-to-pulse Doppler shift corresponding to the turbine rotation. (See also the discussion below.) As before, the complex reflectivity (4.15) leads to scintillation.

4.2.3. STFT for rotating blade. It is often noted that time-frequency analysis of wind turbines shows characteristic oscillatory features. We see this oscillatory behavior in Figure 2, for example. Here we carry out an STFT analysis of (4.14) that explains this behavior.

We assume the microfluctuations $\mathcal{T}$ may be neglected, and that the ambiguity function A is constant over the support of the scatterer B. Then d_p^B may be approximated as

$$d^B[p] \propto \int B(\boldsymbol{z}) e^{i2k_c \boldsymbol{x}^0 \cdot \mathcal{O}_{pT}^{-1} \boldsymbol{z}} d\boldsymbol{z}. \tag{4.16}$$

We expand $\mathcal{O}_t^{-1}$ about the time $t = mT$: $\mathcal{O}_t^{-1} = \mathcal{O}_{mT}^{-1} + \dot{\mathcal{O}}_{mT}^{-1}(t - mT) + \cdots$. Then, to first order,

$$d^B[p] \propto \int B(\boldsymbol{z}) e^{i2k_c \boldsymbol{x}^0 \cdot \mathcal{O}_{mT}^{-1} \boldsymbol{z}} e^{i2k_c \boldsymbol{x}^0 \cdot \dot{\mathcal{O}}_{mT}^{-1} \boldsymbol{z}(p-m)T} d\boldsymbol{z} \tag{4.17}$$

$$\propto \int B(\boldsymbol{z}) e^{i2k_c \boldsymbol{x}^0 \cdot \mathcal{O}_{mT}^{-1} \boldsymbol{z}} e^{i\theta_m(\boldsymbol{z})(p-m)} d\boldsymbol{z}, \tag{4.18}$$

where $\theta_m(\boldsymbol{z}) = 2k_c T \boldsymbol{x}^0 \cdot \dot{\mathcal{O}}_{mT}^{-1} \boldsymbol{z}$. We see that for each scatterer $\boldsymbol{z}$, $\theta_m(\boldsymbol{z})$ varies in a sinusoidal manner with the slow-time index m. In particular, $\dot{\mathcal{O}}_{mT}^{-1} \boldsymbol{z}$ corresponds to the angular velocity of the scattering point $\boldsymbol{z}$. Consequently the length-R discrete-time Fourier transform with respect to the discrete variable p is

$$\begin{aligned} &D_m(e^{i\theta}) \\ &= \sum_{p=m}^{m+R-1} d^B[p] e^{-i\theta p} \propto \int B(\boldsymbol{z}) e^{i2k_c \boldsymbol{x}^0 \cdot \mathcal{O}_{mT}^{-1} \boldsymbol{z}} e^{i(\theta - \theta_m(\boldsymbol{z})(R-1)/2} \frac{\sin((\theta - \theta_m(\boldsymbol{z}))P/2)}{\sin((\theta - \theta_m(\boldsymbol{z}))/2)} d\boldsymbol{z}. \end{aligned} \tag{4.19}$$

From (4.19) we see that the rotating blades correspond to completely different behavior in the time-frequency plane from the behavior exhibited by the target (4.8). Instead of a peak in the spectrum at angular frequency $\theta = \Theta = 2k_c vT$ for a translating target of down-range velocity v, each visible scatterer $\boldsymbol{z}$ on the rotating blades gives rise to peaks at $\theta_m(\boldsymbol{z}) = 2k_c T \boldsymbol{x}^0 \cdot \dot{\mathcal{O}}_{mT}^{-1} \boldsymbol{z}$, and these peaks move sinusoidally with the slow-time index m. (See Figure 2. The horizontal axis corresponds to m and the vertical axis corresponds to θ.) We see parts of the sinusoid only at those slow times when the scatterer is visible. Thus, for example, in some cases we see a large part of a sinusoid from the blade tip. Other parts of the scatterer may be visible for only very short times (for example, the blade flash when the blade is vertical); these visibility effects are excluded from this model by our use of the Born approximation.

4.2.4. Statistical properties of backscattered return from rotating object. Define $C(p, p')$ to be the correlation between the output d_p^B for pulse p, and the output $d_{p'}^B$ for pulse p':

$$C(p, p') \doteq \mathbb{E}[d^B[p](d^B[p'])^*], \tag{4.20}$$

where $\mathbb{E}$ denotes expectation.

Theorem 1 (below) establishes that this function is periodic in each of the variables p and p', which is to say the sequence $\{d_p^B\}$ is periodically correlated, or second-order cyclostationary.

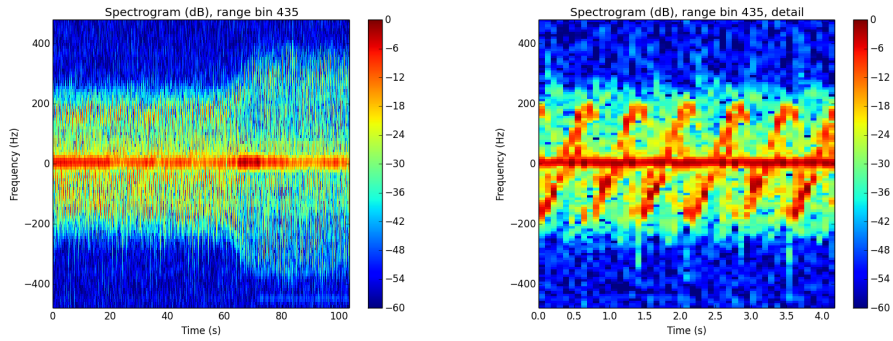

FIG. 2. *(Left) STFT of the signal from range bin* 435. *(Right) Detailed STFT of signal from range bin* 435 *over two full periods of turbine rotation, or approximately* 4.18 *s. The STFT was generated with a sliding Kaiser window* ($\alpha = 1.5$) *supported on forty pulses with an overlap of twenty pulses.*

THEOREM 1. When $\mathcal{T}$ is stationary and a full rotation corresponds to an integral number P of radar pulses, the radar data given by (4.11) are second-order cyclostationary.

Proof. We compute the autocorrelation

$$
\begin{aligned}
C(p+P, p+P') &= \mathbb{E}\left[d^B[p+P](d^B[p'+P])^*\right] \\
&\propto \mathbb{E}\left[\int q_{(p+P)T}(\boldsymbol{z}) e^{2ik_c\hat{\boldsymbol{x}}^0\cdot\mathcal{O}^{-1}_{(p+P)T}\boldsymbol{z}} d\boldsymbol{z} \int q^*_{(p'+P)T}(\boldsymbol{z}') e^{-2ik_c\hat{\boldsymbol{x}}^0\cdot\mathcal{O}^{-1}_{(p'+P)T}\boldsymbol{z}'} d\boldsymbol{z}'\right] \\
&= \int \mathbb{E}[q_{(p+P)T}(\boldsymbol{z}) q^*_{(p'+P)T}(\boldsymbol{z}')] e^{2ik_c\hat{\boldsymbol{x}}^0\cdot(\mathcal{O}^{-1}_{pT}-\mathcal{O}^{-1}_{p'T})\boldsymbol{z}} d\boldsymbol{z} d\boldsymbol{z}',
\end{aligned} \tag{4.21}
$$

where $\mathbb{E}$ denotes expectation and where, for convenience, we have dropped the superscript B on q^B_p. From (4.15), we see that the expectation in the last line of (4.21) is

$$
\begin{aligned}
&\mathbb{E}[q_{(p+P)T}(\boldsymbol{z}) q^*_{(p'+P)T}(\boldsymbol{z}')] \\
&\quad = \mathbb{E}\left[B(\boldsymbol{z})\, e^{2ik_c\mathcal{T}((p+P)T,(\mathcal{O}^{-1}_{(p+P)T}\boldsymbol{z}))} B^*(\boldsymbol{z})\, e^{-2ik_c\mathcal{T}((p'+P)T,(\mathcal{O}^{-1}_{(p'+P)T}\boldsymbol{z}'))}\right] \\
&\quad = \mathbb{E}\left[B(\boldsymbol{z})\, e^{2ik_c\mathcal{T}((p+P)T,(\mathcal{O}^{-1}_{pT}\boldsymbol{z}))} B^*(\boldsymbol{z})\, e^{-2ik_c\mathcal{T}((p'+P)T,(\mathcal{O}^{-1}_{p'T}\boldsymbol{z}'))}\right] \\
&\quad = \mathbb{E}\left[B(\boldsymbol{z})\, e^{2ik_c\mathcal{T}(pT,(\mathcal{O}^{-1}_{pT}\boldsymbol{z}))} B^*(\boldsymbol{z})\, e^{-2ik_c\mathcal{T}(p'T,(\mathcal{O}^{-1}_{p'T}\boldsymbol{z}'))}\right] = \mathbb{E}[q_{pT}(\boldsymbol{z}) q^*_{p'T}(\boldsymbol{z}')].
\end{aligned} \tag{4.22}
$$

This ensures the autocorrelation $C(p, p')$ of the sequence $\{d^B_p\}$ is periodic in each of the variables p and p', which is to say the sequence is cyclostationary with period P. ∎

We shall make no further assumptions about the functional form of C, for to do so would be to presume more information about the scattering correlation $\mathbb{E}[q_{pT}(\boldsymbol{z}) q^*_{p'T}(\boldsymbol{z}')]$ than can be known for a random scatterer such as a wind turbine.

4.3. Target and clutter model assumptions. Our approach will be to model the second-order statistics for clutter, and the first-order statistics for target, so that an ACE statistic [34, 18, 19] may be computed as the score assigned to each cell of the range-Doppler plane.

4.3.1. Constant velocity target. We have assumed that the target has a constant down-range velocity v over the observation time, which means that the phase $\theta^X[p]$ advances linearly in pulse number p. In addition, we have assumed the scintillating reflectivity $\beta^X[p] = \int q_p^X(\boldsymbol{z})d\boldsymbol{z}$ is constant over R pulses, after which phase coherence is lost. Thus we organize the sequence of pulses into pulse trains, each pulse train consisting of R pulses. Over each pulse train the phase of $d^X[p]$ advances linearly. At the end of R pulses, a new pulse train begins. The resulting set of $P = \mathcal{M}R$ pulses accounts for the number of pulses transmitted and received in 1/3 of a turbine period.

We parameterize the index for the pth transmitted pulse on the time interval $[0, \mathcal{M}RT]$ as $p = mR + r$. That is, p denotes the rth pulse in the mth pulse train. Thus, for the pulse $p = mR + r$, the part of the signal due to the linearly translating target is

$$d^X[mR + r] = \beta_m e^{ir\Theta}, \tag{4.23}$$

where the phase increment is $\Theta = 2k_c vT$ and where we have written $\beta_m \doteq \beta^X[m]$.

For unaliased resolution of v (which is our objective), the phase advance Θ per pulse must be less than or equal to 2π, which is to say,

$$|2k_c vT| \leq 2\pi \quad \text{or} \quad |vT| \leq \frac{\pi}{k_c} = \frac{\lambda_c}{2}, \tag{4.24}$$

where $\lambda_c = 2\pi/k_c$ is the wavelength at the carrier frequency $f_c = \omega_c/(2\pi)$. That is, the target must not travel more than a half-wavelength $\lambda_c/2$ of the carrier wave between pulse transmissions. This places a constraint on the radar design: for example, a carrier frequency corresponding to a wavelength of $\lambda_c = 10$ cm and a pulse repetition rate of 1 KHz has a maximum unambiguous velocity of 50 m/sec, or a maximum unambiguous velocity range of ± 25 m/sec.

4.3.2. Wind turbine. For the period P of the cyclostationary clutter, we assume $P = \mathcal{M}R$, where R is the number of pulses over which the phase of $d^X[p]$ changes linearly. Thus P is the total number of pulses transmitted in 1/3 of a wind turbine rotation, after which the wind turbine returns to its original position, and the correlation function of the scatterers repeats. This means we may assemble the correlations between $P = \mathcal{M}R$ pulses into the correlation matrix $\boldsymbol{R}$:

$$\boldsymbol{R} = \begin{pmatrix} C[1,1] & C[1,2] & \cdots & C[1,\mathcal{M}R] \\ C[2,1] & C[2,2] & \cdots & C[2,\mathcal{M}R] \\ \vdots & \vdots & & \vdots \\ C[\mathcal{M}R,1] & C[\mathcal{M}R,2] & \cdots & C[\mathcal{M}R,\mathcal{M}R] \end{pmatrix}. \tag{4.25}$$

By way of example, for the system described in section 6, $T = 1$ msec, and the wind turbine, which has 3 (assumed identical) blades, undergoes a full rotation about every 2 sec. Consequently the number of pulses in 1/3 of a turbine rotation is about 2000/3. Thus for $R = 20$ and $\mathcal{M}RT = 2/3$ sec, the resulting value of $\mathcal{M}$ is $\mathcal{M} = 100/3 \approx 33$. So by organizing radar returns into blocks of $33 \cdot 20 = 660$ pulses, we may treat each such consecutive block as if its clutter component had the same correlation structure as every other such block. This reasoning holds for clutter from a single turbine, but not for multiturbine wind farms, unless the turbines all rotate at the same angular rate.

5. Target detector. In this section, we give a more complete explanation of the material summarized in [27]. Motivated by the discussion in section 4.3, in the range

bin at delay $\tau = 2|\boldsymbol{x}^0|/c$ that corresponds to a wind turbine, we organize the radar returns into groups of R sequential pulses. We refer to each group as a "pulse train." We denote the mth pulse train by the column vector $\boldsymbol{y}_m \in \mathbb{C}^R$, so that the data in the wind turbine range bin, for a 1/3 rotation of a 3-bladed wind turbine, are written $\boldsymbol{y} = [\boldsymbol{y}_0^T, \boldsymbol{y}_1^T, \ldots, \boldsymbol{y}_{\mathcal{M}-1}^T]^T \in \mathbb{C}^{\mathcal{M}R}$, where the superscript T denotes transpose.

With the data for the wind turbine range bin organized in this manner, we consider possible methods for detecting the linearly moving target in the same range bin as the wind turbine. By a target detector [33], we mean a method for choosing between two hypotheses, namely, hypothesis H_0 that the radar return $\boldsymbol{y}$ consists only of radar returns from the wind turbine, versus hypothesis H_Θ that $\boldsymbol{y}$ consists of radar returns from a linearly moving target with hypothesized velocity $v = \Theta/(2k_cT)$ in addition to returns from the wind turbine. The method for choosing between the two hypotheses depends on combining the data $\boldsymbol{y}$ to form a scalar "test statistic," which is then compared to a threshhold. If the test statistic is above the threshhold, hypothesis H_Θ is chosen and the target is said to be detected; otherwise, hypothesis H_0 is chosen and the method concludes that no target is present.

The first step in the construction of a detector is the development of a complex, proper, multivariate normal model for the data, where the target signature enters the mean and the clutter correlation enters the covariance.

As outlined in section 4.3, we assume that the target return is an incoherent sequence of $\mathcal{M}$ coherent pulse trains, each of which consists of R phase-coherent pulses. In other words, we do not enforce phase continuity between consecutive pulse trains. We do, however assume that the target remains in the same range bin and has constant velocity over MR pulses, where M is an integer $M \leq \mathcal{M}$. Based on (4.23), we denote the target return for the mth train as

$$\boldsymbol{\psi}_R(\Theta)\beta_m, \quad m = 0, 1, \ldots, M-1, \tag{5.1}$$

where $\boldsymbol{\psi}_R(\Theta) = [1, e^{i\Theta}, \ldots, e^{i(R-1)\Theta}]^T \in \mathbb{C}^R$ and β_m is the target reflectivity (4.7) at the beginning of the mth pulse train. The parameters β_m and Θ are unknown. Consequently we hypothesize the distribution of $\boldsymbol{y}$ under each hypothesis as

$$\begin{aligned} H_0 &: \boldsymbol{y} \sim \mathcal{CN}_{MR}(\boldsymbol{0}, \boldsymbol{R}), \\ H_\Theta &: \boldsymbol{y} \sim \mathcal{CN}_{MR}(\boldsymbol{\beta} \otimes \boldsymbol{\psi}_R(\Theta), \boldsymbol{R}), \end{aligned} \tag{5.2}$$

where $\boldsymbol{\beta} = [\beta_0, \beta_1, \ldots, \beta_{M-1}]^T \in \mathbb{C}^M$ are the unknown overall target reflectivities (4.7) for each pulse train, using the notation introduced in (4.23), and using $\otimes$ to denote Kronecker product. Here we have assumed that the wind turbine returns have zero mean and covariance $\boldsymbol{R}$ given by (4.25). Because the target parameters $\boldsymbol{\beta}$ and Θ are unknown, our strategy will be to consider this a subspace detection problem, in which we seek a detection statistic invariant to $\boldsymbol{\beta}$. Our statistic will depend on Θ; we will seek to maximize the detection statistic as a function of Θ.

In order to fix notation (see Table 1), we give $\boldsymbol{R}$ the following pattern:

$$\boldsymbol{R} = \begin{bmatrix} \boldsymbol{R}_{00} & \boldsymbol{R}_{01} & \cdots & \boldsymbol{R}_{0(M-1)} \\ \boldsymbol{R}_{01}^H & \boldsymbol{R}_{11} & \cdots & \boldsymbol{R}_{1(M-1)} \\ \vdots & & \ddots & \vdots \\ \boldsymbol{R}_{0(M-1)}^H & \cdots & \cdots & \boldsymbol{R}_{(M-1)(M-1)} \end{bmatrix}. \tag{5.3}$$

The covariance block $\boldsymbol{R}_{mn} \in \mathbb{C}^{R\times R}$ is $\boldsymbol{R}_{mn} = \mathbb{E}[\boldsymbol{y}_m\boldsymbol{y}_n^H]$ for $m, n \in \{0, 1, \ldots, M-1\}$.

TABLE 1
Notation summary.

R	Number of pulses in a pulse train (over which target is phase coherent)
$\mathcal{M}$	Number of (R-pulse) pulse trains in a clutter period
$P = \mathcal{M}R$	Number of pulses in a clutter period
K	Number of pulse trains in a clutter block = separation of number of pulse trains over which clutter is uncorrelated
KR	Number of pulses in a clutter block
M	Number of pulse trains over which target stays in range bin ($M \leq \mathcal{M}$) = number of pulse trains used in a detector
$N = M/K$	Number of uncorrelated clutter blocks in a detector statistic

We make the assumption that $\boldsymbol{R}$ is block diagonal with N blocks of size KR, and $NKR = MR$. So, there are N blocks on the diagonal, each of size $KR \times KR$. Then, we have

$$\boldsymbol{R} = \text{blkdiag}[\boldsymbol{Q}_{00}, \boldsymbol{Q}_{11}, \ldots, \boldsymbol{Q}_{(N-1)(N-1)}], \tag{5.4}$$

where $\boldsymbol{Q}_{nn} = \mathbb{E}[\boldsymbol{w}_n \boldsymbol{w}_n^H] \in \mathbb{C}^{KR \times KR}$ under H_0, and $\boldsymbol{w}_n^T = [\boldsymbol{y}_{nK}^T, \ldots, \boldsymbol{y}_{(n+1)K-1}^T]^T$. This model amounts to an approximation that clutter is uncorrelated for pulse trains separated by more than K trains. With this block-diagonal approximation, $\boldsymbol{w}_n$'s are independent for $n \in \{0, \ldots, N-1\}$, each distributed as

$$\begin{aligned} H_0 &: \boldsymbol{w}_n \sim \mathcal{CN}_{KR}(\boldsymbol{0}, \boldsymbol{Q}_{nn}), \\ H_\Theta &: \boldsymbol{w}_n \sim \mathcal{CN}_{KR}(\boldsymbol{\beta}_n \otimes \boldsymbol{\psi}_R(\Theta), \boldsymbol{Q}_{nn}), \end{aligned} \tag{5.5}$$

and $\boldsymbol{\beta}_n = [\beta[nK], \ldots, \beta[(n+1)K-1]]^T \in \mathbb{C}^K$.

The mean under hypothesis H_Θ may be written as

$$\boldsymbol{\beta}_n \otimes \boldsymbol{\psi}_R(\Theta) = \boldsymbol{\Psi}_{KR}(\Theta)\boldsymbol{\beta}_n, \tag{5.6}$$

where $\boldsymbol{\Psi}_{KR}(\Theta) = \mathbf{I}_K \otimes \boldsymbol{\psi}_R(\Theta) \in \mathbb{C}^{KR \times K}$. Thus, the hypothesis test for the random vectors $\boldsymbol{w}_0, \ldots, \boldsymbol{w}_{N-1}$ may be written as

$$\begin{aligned} H_0 &: \boldsymbol{w}_n \sim \mathcal{CN}_{KR}(\boldsymbol{0}, \boldsymbol{Q}_{nn}), \\ H_\Theta &: \boldsymbol{w}_n \sim \mathcal{CN}_{KR}(\boldsymbol{\Psi}_{KR}(\Theta)\boldsymbol{\beta}_n, \boldsymbol{Q}_{nn}), \end{aligned} \tag{5.7}$$

where $n = 0, 1, \ldots, N-1$ and $N = M/K$. This is the basic hypothesis-testing model for which we derive a generalized likelihood ratio test.

The detection strategy is to construct a test statistic Λ_{LR} that consists of a likelihood ratio

$$\Lambda_{LR} = \frac{f_\Theta(\boldsymbol{w})}{f_0(\boldsymbol{w})}, \tag{5.8}$$

where $f_i(\boldsymbol{w})$ is the probability density function (pdf) of $\boldsymbol{w}$ under hypothesis $i = 0$ or Θ. Because of the assumed independence of the $\boldsymbol{w}_n$, each pdf f_i can be written as a product of the corresponding pdfs $f_{i,n}$ for each n:

$$\Lambda_{LR} = \prod_{n=0}^{N-1} \frac{f_{\Theta,n}(\boldsymbol{w}_n)}{f_{0,n}(\boldsymbol{w}_n)}, \tag{5.9}$$

where $F_i(\boldsymbol{w}) = \prod f_{i,n}(\boldsymbol{w}_n)$. Thus the test statistic Λ_{LR} can be written as a product of the N likelihood ratios for each $\boldsymbol{w}_n$.

The challenge in computing (5.9) is that the pdfs $f_{\Theta,n}$ and $f_{0,n}$ contain the unknown parameters $\boldsymbol{Q}_{nn}$ and $\boldsymbol{\beta}_n$. By replacing the unknowns under each hypothesis with their maximum likelihood (ML) estimates, we derive the generalized likelihood ratio test for this problem, under two alternative assumptions.

5.1. MPCE. In the first approach, we assume that the WTC samples from each pulse are independent and, consequently, $\boldsymbol{Q}_{nn} = \sigma_n^2 \boldsymbol{I}$, where $\boldsymbol{I}$ denotes the $KR \times KR$ identity matrix. In this case, we need to determine ML estimates of only σ_n^2 and $\boldsymbol{\beta}_n$. Thus

$$\Lambda_{MPCE} = \prod_{n=0}^{N-1} \frac{\max_{\sigma_n^2, \boldsymbol{\beta}_n} f_{\Theta,n}(\boldsymbol{w}_n)}{\max_{\sigma_n^2} f_{0,n}(\boldsymbol{w}_n)}. \tag{5.10}$$

This calculation is carried out in Appendix A. The result is

$$\Lambda_{MPCE} = \prod_{n=0}^{N-1} \frac{1}{(1-\eta_n^2)^{KR}}, \qquad \text{where} \qquad \eta_n^2 = \frac{|\boldsymbol{P}_{\boldsymbol{\Psi}} \boldsymbol{w}_n|^2}{|\boldsymbol{w}_n|^2}, \tag{5.11}$$

where $\boldsymbol{P}_{\boldsymbol{\Psi}} = \boldsymbol{\Psi}(\boldsymbol{\Psi}^H \boldsymbol{\Psi})^{-1} \boldsymbol{\Psi}^H$ denotes the orthogonal projection onto the range of $\boldsymbol{\Psi} = \boldsymbol{\Psi}_{KR}(\Theta)$. [Here the superscript H denotes (Hermitian) conjugate transpose.] The ratio η_n^2 thus has the geometrical interpretation of being the square of the cosine of the angle between $\boldsymbol{w}_n$ and the subspace spanned by $\boldsymbol{\Psi}_{KR}(\Theta)$.

A monotone function of Λ_{MPCE} is

$$1 - \frac{1}{(\Lambda_{MPCE})^{1/(KR)}} = 1 - \prod_{n=0}^{N-1} (1-\eta_n^2). \tag{5.12}$$

Because $0 \le \eta_n^2 \le 1$, this detector test statistic ranges between 0 and 1.

5.2. MPACE. An alternative approach is to exploit any available training data to estimate the unknown clutter correlation. In particular, we assume that we can obtain a training sample of L copies of $\boldsymbol{z}_l \sim \mathcal{CN}_{MR}(\boldsymbol{0}, \boldsymbol{R}_{zz})$ under H_0, i.e., samples of radar returns from the wind turbine only, where

$$\boldsymbol{R}_{zz} = \text{blkdiag}[\sigma_0^2 \boldsymbol{Q}_{00}, \sigma_1^2 \boldsymbol{Q}_{11}, \ldots, \sigma_{(N-1)}^2 \boldsymbol{Q}_{(N-1)(N-1)}] \tag{5.13}$$

for some unknown set of relative scalings $\{\sigma_0^2, \sigma_1^2, \ldots, \sigma_{N-1}^2\}$. We assume that $L \ge KR$. Partitioning the training data matrix as $\boldsymbol{Z} = [\boldsymbol{z}_0, \ldots, \boldsymbol{z}_{L-1}] = [\boldsymbol{Z}_0^T, \ldots, \boldsymbol{Z}_{N-1}^T]^T$, $\boldsymbol{Z}_n \in \mathbb{C}^{KR \times L}$, we find that the generalized likelihood ratio (GLR) [33] for the hypothesis test in (5.7) is

$$\Lambda_{GLR} = \frac{\max_{\{\sigma_n^2, \beta_n, \boldsymbol{Q}_{nn}\}_{n=0}^{N-1}} f_{H_\Theta}(\boldsymbol{W}, \boldsymbol{Z})}{\max_{\{\sigma_n^2, \boldsymbol{Q}_{nn}\}_{n=0}^{N-1}} f_{H_0}(\boldsymbol{W}, \boldsymbol{Z})}, \tag{5.14}$$

where the pdfs $f_{H_0}(\boldsymbol{W}, \boldsymbol{Z})$ and $f_{H_\Theta}(\boldsymbol{W}, \boldsymbol{Z})$ are the joint pdfs of the test data $\boldsymbol{W} = [\boldsymbol{w}_0, \ldots, \boldsymbol{w}_{N-1}]$ under H_0 and H_1, respectively, and the training data $\boldsymbol{Z} = [\boldsymbol{Z}_0^T, \ldots, \boldsymbol{Z}_{N-1}^T]^T$. The assumption (5.4) allows us to write (5.14) as

$$\Lambda_{GLR} = \prod_{n=0}^{N-1} \frac{\max_{\sigma_n^2, \beta_n, \boldsymbol{Q}_{nn}} f_{H_\Theta}(\boldsymbol{w}_n, \boldsymbol{Z}_n)}{\max_{\sigma_n^2, \boldsymbol{Q}_{nn}} f_{H_0}(\boldsymbol{w}_n, \boldsymbol{Z}_n)}. \tag{5.15}$$

As in the MPCE case, each factor of (5.15) can be written using the results in [17, 18, 19], by replacing the unknown parameters $\{\sigma_n^2, \boldsymbol{\beta}_n, \boldsymbol{Q}_{nn}\}_{n=0}^{N-1}$ with their ML estimates under each hypothesis. The result is

$$\Lambda_{GLR} = \prod_{n=0}^{N-1} \frac{1}{(1-\rho_n^2)^{KR}}, \tag{5.16}$$

where $\rho_n^2 = \frac{\boldsymbol{v}_n^H \boldsymbol{P}_{\boldsymbol{G}_n} \boldsymbol{v}_n}{\boldsymbol{v}_n^H \boldsymbol{v}_n}$ is the ACE score, $\boldsymbol{v}_n = \widehat{\boldsymbol{Q}}_{nn}^{-1/2} \boldsymbol{w}_n$ is a whitened version of $\boldsymbol{w}_n$, where $\widehat{\boldsymbol{Q}}_{nn} = \frac{1}{L} \boldsymbol{Z}_n \boldsymbol{Z}_n^H$ is the sample covariance matrix for the nth block, $\boldsymbol{G}_n = \widehat{\boldsymbol{Q}}_{nn}^{-1/2} \boldsymbol{\Psi}_{KR}(\Theta)$, and $\boldsymbol{P}_{\boldsymbol{G}_n}$ denotes the projection operator onto the subspace spanned by $\boldsymbol{G}_n$. The quantity ρ_n^2, which can also be written

$$\rho_n^2 = \frac{|\boldsymbol{P}_{\boldsymbol{G}_n} \boldsymbol{v}_n|^2}{|\boldsymbol{v}_n|^2}, \tag{5.17}$$

is the square of the cosine of the angle between the whitened vector $\boldsymbol{v}_n$ and the subspace spanned by the whitened $\boldsymbol{G}_n$. Details of the derivation of (5.16) are given in the appendix.

We call the detector test statistic of (5.16) MPACE. It is a product of $N = M/K$ sine-squared terms, and each sine-squared term is one minus an ACE score, which is itself a coherence score.

A monotone function of Λ_{GLR} is

$$1 - \left(\frac{1}{\Lambda_{GLR}}\right)^{1/(KR)} = 1 - \left(\prod_{n=0}^{N-1} (1-\rho_n^2)^{KR}\right)^{1/(KR)} = 1 - \prod_{n=0}^{N-1} (1-\rho_n^2). \tag{5.18}$$

Because $0 \le \rho_n^2 \le 1$, this detector test statistic ranges between 0 and 1.

Note that we are free to choose R, K, and M in our experiments. Therefore, the MPACE detector consists of the product of $N = M/K$ time-domain ACE scores, ρ_n^2, each of which processes K pulse trains of duration R to form a cosine-squared statistic [34, 18, 19]. These scores have the virtue that they are invariant to scalings of the target signature $\boldsymbol{\psi}$, and of the time-domain blocks of data $\boldsymbol{w}_n$. The detector in (5.16) is derived based on the approximation of $\boldsymbol{R}$ by a block-diagonal matrix with blocks of size KR for some $1 \le K \le M \le \mathcal{M}$.

The choice of the three parameters R, M, and K must be selected by the designer based on experimental evidence. A more detailed discussion of the parameter choice, together with an alternative frequency-domain approach, can be found in [27].

6. Results. In this section, we summarize the results in [27] of testing the detector of section 5 on real data.

We obtained a set of S-band, dual-polarization data from the CSU-CHILL National Weather Radar Facility located in Greeley, Colorado and operated by Colorado State University. The system operates at a center frequency of $f_c = 2.725$ GHz, which corresponds to a wavelength λ_c of 11 cm. The pulse repetition interval T is 1.042 msec ≈ 1 msec, and the system has 1 MHz bandwidth, which corresponds to a pulse duration of 1 μsec $= 10^{-6}$ sec. The transmitted waveforms are "continuous-wave" pulses, meaning that w of (3.1) is approximately a characteristic function of duration 1 μsec. We used $99349 \approx 10^5$ pulses. This means the total data record has duration $\approx 10^5$ pulses $\times 10^{-3}$ sec/pulse $= 100$ sec. The CHILL radar system recorded returns with a maximum range of 75 km, aggregated into 500 range bins, each 150 m wide.

Figure 1 shows the layout of the Ponnequin wind farm, with iso-range curves superimposed. The figure also shows the 150 m range bins and .1° beam demarcations. The beam width for the S-band radar data that we are using is 1°, so ten boxes correspond to the width of the beam. There are 4 lines of wind turbines totaling 44.

The radar was pointed towards the Ponnequin wind farm, about 63 km away. Although the wind farm contains both NEG and Vestas turbines, we focused our attention on range bin 435, which we believe contains only a single Vestas turbine. The Vestas turbines (model 47) rotate at only a single nonzero rate, namely, 29 rpm. The blades are 77 feet long, and the pivot is 227 feet above the ground. These operate at a constant blade pitch while the blades are moving.

In Figure 2 we show the STFT of the pulse history of the 435th range bin. It exhibits the characteristic periodicity associated with clutter from a wind turbine. After approximately 65 sec, the orientation of the wind turbine changed, increasing the Doppler extent of the clutter. Empirically, the turbine period is 2.091 sec (≈ 2007 pulses), which is reasonably close to the turbine's nominal operating frequency of 29 rpm.

We caution the reader that Figure 2 is used for qualitative insight only. Nowhere in our theory do we use an STFT of the data to implement our detectors. Moreover, our only use of cyclostationarity is to argue that the correlation structure of the WTC repeats itself every $\mathcal{M}R$ pulses.

In addition, we obtained an additional set of data recorded using the CSU-CHILL platform which observed an unidentified aircraft passing through its line of sight with minimal stationary clutter. This aircraft seemed to be on an approach to Denver International Airport. These data was recorded with the same system parameters (center frequency, pulse duration, etc.) as the WTC data. For these data, the maximum unambiguous velocity range is ± 25 m/sec. We superimposed the two pulse histories (aircraft and wind turbine) to obtain the pulse history of a single, synthetic range bin containing both airplane and turbine.

We expect this to be a good approximation[4] to realistic data from an aircraft and wind turbine at the same range. The airplane's signal-to-noise ratio is approximately -25.7 dB relative to the turbine. The target is present in the range bin in question for approximately two seconds, starting about 23 seconds into the dataset, likely moving at a nominal velocity of -70 m/sec (an inference from public flight records and from our experimental data). As this is outside the maximum unambiguous velocity range, we observe instead an aliased copy of the airplane at an apparent velocity of -20 m/sec.

The data were divided into a training set (≈ 9 turbine periods) and a test set (≈ 15 turbine periods). The training period was the final 18 seconds and the test period was the initial 31 seconds. From Figure 2 we see that the training was done while the wind turbine was oriented differently from the test data.

We compared the MPACE detector (5.16) to its nonadaptive counterpart MPCE, in which we replace $\boldsymbol{R}$ by the identity matrix. In Figure 3, we plot the MPCE and MPACE detector scores for each hypothesized velocity (vertical axis). In both figures, a resolution cell has dimensions $\lambda_c/(RT)$ m/sec in velocity and MRT sec in time. We see that that the airplane is rendered nearly undetectable by the nonadaptive MPCE. The MPACE detector, however, is able to separate the target from the clutter. Here we used $R = 17$ and $K = 1$. We see that the coherence detector

[4]Airplanes and turbines are typically far enough arpart that multiple scattering between them is unlikely and even if present would appear in a different range bin.

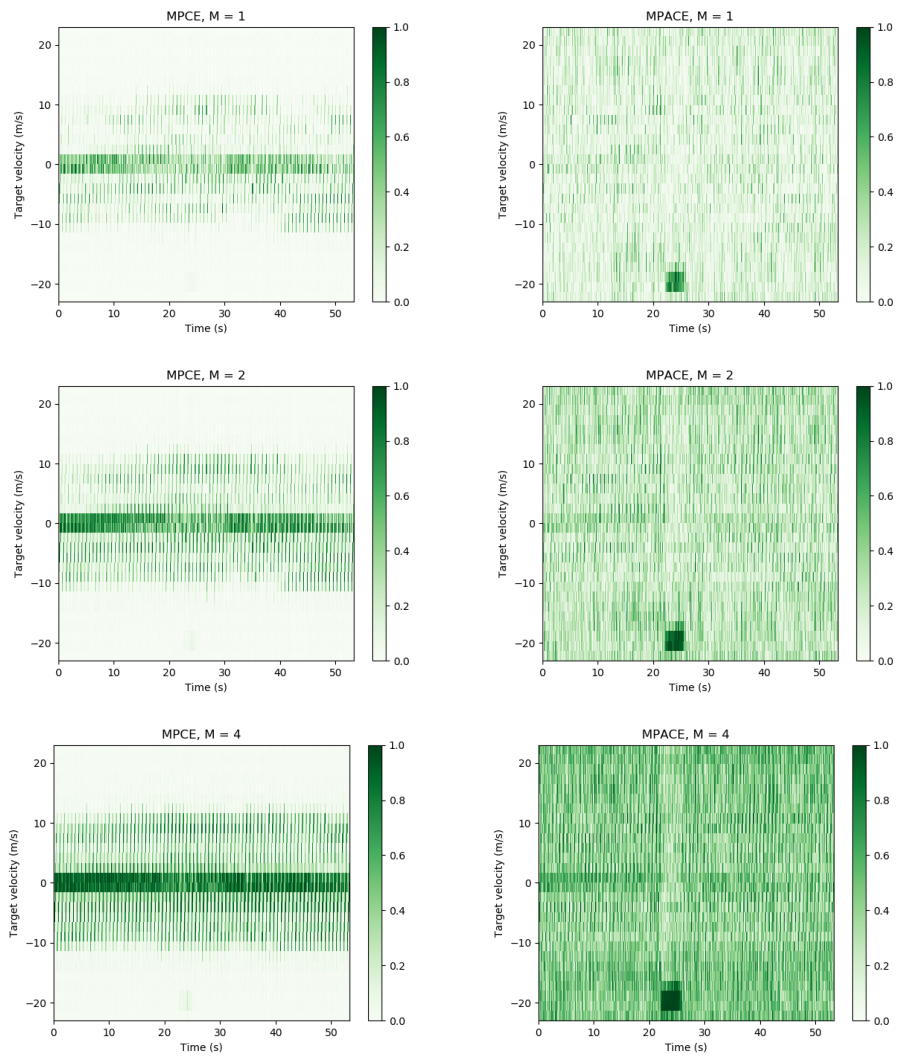

FIG. 3. *MPCE detection (left) compared with MPACE detection (right) for* $K = 1$ *and* $M = 1, 2, 4$.

distributes clutter power evenly over the entire Doppler plane by whitening, whereas the matched filter leaves the WTC power distributed unevenly within its Doppler extent.

In Figure 4, we plot slices through the plots of Figure 3 at the expected (aliased) target velocity in order to demonstrate detection and range resolution.

7. Conclusions. In this paper we have derived a measurement model for target and clutter in a pulse-Doppler radar system. The model has three design parameters: R, the number of consecutive pulses over which baseband phase increases linearly in response to a constant velocity target; M, the number of such R-pulse trains over which a target remains in a given range bin at a fixed velocity; and K, the parameter that models the $MR \times MR$ wind clutter covariance as a block-diagonal matrix of N different $KR \times KR$ blocks. The assumption that the clutter covariance is uncorrelated over pulses sequences of length greater than K may be a particularly

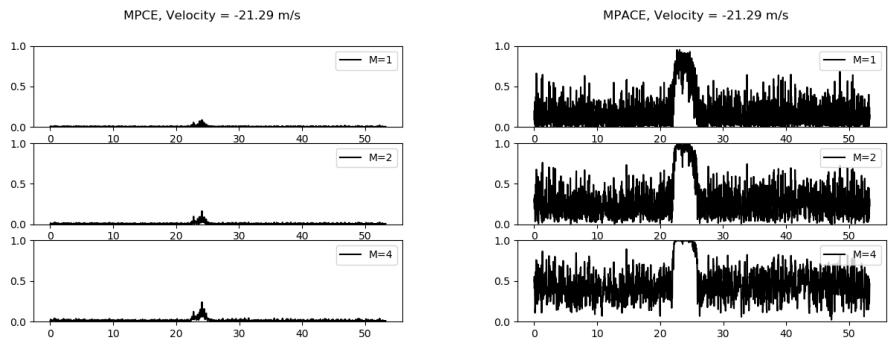

FIG. 4. *Slices through Figure* 3.

appropriate approximation in the case of a scanning radar, with which we see the target and clutter only for short periods during each rotation of the radar.

This measurement model is then used to derive a GLR test. This test is a threshold test that uses a bulk coherence statistic, consisting of an incoherent geometric average of coherently computed ACE scores. Each ACE score is an ACE between an R-dimensional measurement and a K-dimensional subspace of $\mathbb{C}^R$. The R-dimensional measurement is the output of R consecutive range-compressed samples.

Experimental results demonstrate that the coherence detector approximately whitens WTC and detects -25 dB targets embedded in the dominant clutter band of the wind turbine.

We leave for future work the following issues:

- extension of this work to the important case of a wind farm with multiple turbines;
- thorough study of the sensitivity to the parameters R, K, and M and development of methods for their estimation.

Appendix A. MPCE. The numerators of (5.10) have the form

$$\max_{\sigma^2,\boldsymbol{\beta}} f_\Theta(\boldsymbol{w}) = \max_{\sigma^2,\boldsymbol{\beta}} \frac{e^{-|\boldsymbol{w}-\boldsymbol{\Psi}\boldsymbol{\beta}|^2/\sigma^2}}{(\pi\sigma^2)^{KR}}, \tag{A.1}$$

where for notational convenience we have dropped the subscripts n and where σ^2 is the unknown variance of $\boldsymbol{w}-\boldsymbol{\Psi}\boldsymbol{\beta}$. Maximizing (A.1) with respect to σ^2 results in the estimate $\widehat{\sigma}^2 = |\boldsymbol{w}-\boldsymbol{\Psi}\boldsymbol{\beta}|^2/(KR)$. Using $\widehat{\sigma}^2$ back in (A.1) results in

$$\max_{\sigma^2,\boldsymbol{\beta}} f_\Theta(\boldsymbol{w}) = \max_{\boldsymbol{\beta}} \frac{e^{-KR}}{(\pi\widehat{\sigma}^2)^{KR}} = \max_{\boldsymbol{\beta}} \left(\frac{R}{e\pi|\boldsymbol{w}-\boldsymbol{\Psi}\boldsymbol{\beta}|^2}\right)^{KR} \tag{A.2}$$

which is maximized for

$$\widehat{\boldsymbol{\beta}} = \operatorname{argmin}_{\boldsymbol{\beta}} |\boldsymbol{w}-\boldsymbol{\Psi}\boldsymbol{\beta}|^2 = (\boldsymbol{\Psi}^H\boldsymbol{\Psi})^{-1}\boldsymbol{\Psi}^H[\boldsymbol{w}] \tag{A.3}$$

under hypothesis H_Θ. Here the superscript H denotes (Hermitian) conjugate transpose. The corresponding ML estimate under hypothesis H_0 is $\widehat{\boldsymbol{\beta}} = \mathbf{0}$.

The pdf for hypothesis H_Θ is then

$$f_\Theta(\boldsymbol{w}) = \left(\frac{R}{e\pi|\boldsymbol{w}-\boldsymbol{P}_{\boldsymbol{\Psi}}\boldsymbol{w}|^2}\right)^{KR}, \tag{A.4}$$

where $\boldsymbol{P}_{\boldsymbol{\Psi}} = \boldsymbol{\Psi}(\boldsymbol{\Psi}^H\boldsymbol{\Psi})^{-1}\boldsymbol{\Psi}^H$ is the orthogonal projection operator onto the range of $\boldsymbol{\Psi}$. Similarly, the pdf for hypothesis H_0 is

$$f_0(\boldsymbol{w}) \propto \left(\frac{R}{e\pi|\boldsymbol{w}|^2}\right)^{KR}, \tag{A.5}$$

so that the likelihood ratio is

$$\frac{f_\Theta(\boldsymbol{w})}{f_0(\boldsymbol{w})} = \frac{|\boldsymbol{w}|^{2R}}{|\boldsymbol{w}-\boldsymbol{P}_{\boldsymbol{\Psi}}\boldsymbol{w}|^{2KR}} = \left(\frac{\boldsymbol{w}^H\boldsymbol{w}}{\boldsymbol{w}^H(\boldsymbol{I}-\boldsymbol{P}_{\boldsymbol{\Psi}})\boldsymbol{w}}\right)^R = \left(\frac{1}{1-\eta^2}\right)^{KR}, \tag{A.6}$$

where

$$\eta^2 = \frac{\boldsymbol{w}^H\boldsymbol{P}_{\boldsymbol{\Psi}}\boldsymbol{w}}{\boldsymbol{w}^H\boldsymbol{w}}. \tag{A.7}$$

A monotone function of the likelihood ratio is the coherence $\Lambda_C = 1 - \frac{1}{(f_\Theta/f_0)^{1/(KR)}} = \eta^2$.

Appendix B. Derivation of MPACE. This appendix follows [17, 18, 19] and [27]).

In the hypothesis test (5.14), we must find the ML estimates for $\boldsymbol{Q}_{mm}, \sigma_m^2$, and β_m. This is done from the test and training data $\boldsymbol{Z}$. For simplicity we drop the subscripts, and we write the model for the subspace detection problem as

$$\boldsymbol{w} = \boldsymbol{\Psi}\boldsymbol{\beta} + \boldsymbol{n}, \tag{B.1}$$

where $\boldsymbol{w}$ and $\boldsymbol{n} \in \mathbb{C}^{KR}$, $\boldsymbol{\beta} \in \mathbb{C}^K$, and $\boldsymbol{\Psi}$ is a $KR \times K$ complex matrix. The noise $\boldsymbol{n}$ is assumed to be distributed as $\mathcal{CN}(\boldsymbol{0}, \boldsymbol{Q})$. We consider the case in which $\boldsymbol{\Psi}$ is known, but $\boldsymbol{\beta}, \sigma^2$, and $\boldsymbol{Q}$ are all unknown. Hypothesis H_0 corresponds to $\boldsymbol{\beta} = \boldsymbol{0}$; hypothesis H_Θ corresponds to $\boldsymbol{\beta}$ nonzero. Detection of a signal corresponds to deciding H_Θ over H_0.

In order to estimate $\boldsymbol{Q}$, we are given training data $\boldsymbol{Z} = [\boldsymbol{z}_0, \ldots, \boldsymbol{z}_{L-1}]$, where the $\boldsymbol{z}_l \in \mathbb{R}^{KR}$ are mean zero, independent, and identically distributed. Then each $\boldsymbol{z}_l$ is distributed as $\mathcal{CN}(\boldsymbol{0}, \sigma^2\boldsymbol{Q})$, where σ^2 is also unknown. Note that σ^2 here is the unknown scale of the training data, and not the scale of the noise as in the previous appendix.

The pdf for hypothesis H_Θ is

$$\begin{aligned} f_\Theta(\boldsymbol{w}, \boldsymbol{Z}) &= f_\Theta(\boldsymbol{w}) \prod_{l=0}^{L-1} f_\Theta(\boldsymbol{z}_l) = \frac{e^{-(\boldsymbol{w}-\boldsymbol{\Psi}\boldsymbol{\beta})^H\boldsymbol{Q}^{-1}(\boldsymbol{w}-\boldsymbol{\Psi}\boldsymbol{\beta})}}{\pi^{KR}\det(\boldsymbol{Q})} \prod_{l=0}^{L-1} \frac{e^{-\boldsymbol{z}_l^H\boldsymbol{Q}^{-1}\boldsymbol{z}_l/\sigma^2}}{\pi^{KR}\det(\sigma^2\boldsymbol{Q})} \\ &= \frac{1}{(\pi^{KR}\det\boldsymbol{Q})^{L+1}\,(\sigma^2)^{LKR}} \exp\left[-(L+1)\mathrm{Tr}(\boldsymbol{Q}^{-1}\mathbf{M}_\Theta)\right], \end{aligned} \tag{B.2}$$

where the superscript H denotes Hermitian conjugate (conjugate transpose), Tr denotes trace, and where under hypothesis H_Θ, $\mathbf{M}_\Theta$ is the matrix

$$\mathbf{M}_\Theta = \frac{(\boldsymbol{w}-\boldsymbol{\Psi}\boldsymbol{\beta})(\boldsymbol{w}-\boldsymbol{\Psi}\boldsymbol{\beta})^H + \sum_l \boldsymbol{z}_l\boldsymbol{z}_l^H/\sigma^2}{L+1}. \tag{B.3}$$

The pdf for hypothesis H_0 is the same as (B.2) except that $\boldsymbol{\beta} = \boldsymbol{0}$ and $\mathbf{M}_\Theta$ is replaced by $\mathbf{M}_0$ in which $\boldsymbol{\beta} = \boldsymbol{0}$.

The ML estimates for $\boldsymbol{Q}$ under hypotheses H_Θ and H_0 turn out to be equal to $\mathbf{M}_\Theta$ and $\mathbf{M}_0$, respectively. If we replace $\boldsymbol{Q}$ by $\mathbf{M}_\Theta$ and $\mathbf{M}_0$ in the appropriate versions of (B.2), we find that

$$\begin{aligned} f_\Theta(\boldsymbol{w},\boldsymbol{Z})\Big|_{\boldsymbol{Q}=\mathbf{M}_\Theta} &= \frac{e^{-1}}{(\pi^{KR}\det\mathbf{M}_\Theta)^{L+1}\,(\sigma^2)^{LKR}}, \\ f_0(\boldsymbol{w},\boldsymbol{Z})\Big|_{\boldsymbol{Q}=\mathbf{M}_0} &= \frac{e^{-1}}{(\pi^{KR}\det\mathbf{M}_0)^{L+1}\,(\sigma^2)^{LKR}}. \end{aligned} \tag{B.4}$$

The determinant of $\mathbf{M}_\Theta$ and $\mathbf{M}_0$ can be found from the observation that $\det(\mathbf{A}+\boldsymbol{a}\boldsymbol{a}^H) = \det(\mathbf{A})(1+\boldsymbol{a}^H\mathbf{A}^{-1}\boldsymbol{a})$. Taking $\mathbf{A}=\widehat{\boldsymbol{Q}}$, where $\widehat{\boldsymbol{Q}}$ is the sample covariance matrix

$$\widehat{\boldsymbol{Q}} = \frac{1}{L}\sum_{l}^{L} \boldsymbol{z}_l\boldsymbol{z}_l^H, \tag{B.5}$$

we write $\mathbf{M}_\Theta = \frac{L}{(L+1)\sigma^2}\left(\widehat{\boldsymbol{Q}} + \frac{\sigma^2}{L}(\boldsymbol{w}-\boldsymbol{\Psi\beta})(\boldsymbol{w}-\boldsymbol{\Psi\beta})^H\right)$, thus obtaining

$$\det(\mathbf{M}_\Theta) = (\det\widehat{\boldsymbol{Q}})\left(\frac{L}{(L+1)\sigma^2}\right)^{KR}\left(1+\sigma^2\frac{(\boldsymbol{w}-\boldsymbol{\Psi\beta})^H\widehat{\boldsymbol{Q}}^{-1}(\boldsymbol{w}-\boldsymbol{\Psi\beta})}{L}\right) \tag{B.6}$$

and the corresponding result for $\det(\mathbf{M}_0)$ arises from taking $\boldsymbol{\beta}=\mathbf{0}$. Using (B.6) in (B.4) results in

$$\begin{aligned} & f_\Theta(\boldsymbol{w},\boldsymbol{Z})\Big|_{\boldsymbol{Q}=\mathbf{M}_\Theta} \\ &= \frac{e^{-1}}{\left((\det\widehat{\boldsymbol{Q}})\left(\frac{\pi L}{(L+1)\sigma^2}\right)^{KR}\left(1+\sigma^2\frac{(\boldsymbol{w}-\boldsymbol{\Psi\beta})^H\tilde{\boldsymbol{Q}}^{-1}(\boldsymbol{w}-\boldsymbol{\Psi\beta})}{L}\right)\right)^{L+1}(\sigma^2)^{LKR}} \\ &= \frac{e^{-1}(\sigma^2)^{KR}}{\left((\det\widehat{\boldsymbol{Q}})\left(\frac{\pi L}{L+1}\right)^{KR}\right)^{L+1}\left(1+\sigma^2\frac{(\boldsymbol{w}-\boldsymbol{\Psi\beta})^H\widehat{\boldsymbol{Q}}^{-1}(\boldsymbol{w}-\boldsymbol{\Psi\beta})}{L}\right)^{L+1}} \end{aligned} \tag{B.7}$$

and the corresponding result for f_0 is obtained from setting $\boldsymbol{\beta}=0$.

Next we maximize expression (B.4) to obtain the ML estimate for σ^2. We note that f_Θ is proportional to $(\sigma^2)^n(1+\sigma^2 b)^m$, where $n=KR$, $m=-(L+1)$, and $b=(\boldsymbol{w}-\boldsymbol{\Psi\beta})^H\widehat{\boldsymbol{Q}}^{-1}(\boldsymbol{w}-\boldsymbol{\Psi\beta})/L$. The maximum of such an expression occurs at $\sigma^2=\widehat{\sigma}^2_\Theta$, where

$$\widehat{\sigma}^2_\Theta = \frac{-n}{(n+m)b} = \frac{-LKR}{(KR-L-1)(\boldsymbol{w}-\boldsymbol{\Psi\beta})^H\widehat{\boldsymbol{Q}}^{-1}(\boldsymbol{w}-\boldsymbol{\Psi\beta})} \tag{B.8}$$

and the result $\widehat{\sigma}^2_0$ (under hypothesis H_0) is obtained by setting $\boldsymbol{\beta}=\mathbf{0}$.

Substituting (B.8) into (B.7), we find

$$f_\Theta(\boldsymbol{w},\boldsymbol{Z})\Big|_{\boldsymbol{Q}=\mathbf{M}_\Theta} = \frac{e^{-1}(\widehat{\sigma}^2_\Theta)^{KR}}{\left((\det\widehat{\boldsymbol{Q}})\left(\frac{\pi L}{L+1}\right)^{KR}\right)^{L+1}\left(1-\frac{KR}{KR-L-1}\right)^{L+1}} \tag{B.9}$$

and similarly for $\mathbf{M}_0$.

Finally we maximize (B.9) with respect to $\boldsymbol{\beta}$. The maximum is attained at

$$\begin{aligned}\widehat{\boldsymbol{\beta}} &= \operatorname{argmin}_{\boldsymbol{\beta}}(\boldsymbol{w}-\boldsymbol{\Psi\beta})^H\widehat{\boldsymbol{Q}}^{-1}(\boldsymbol{w}-\boldsymbol{\Psi\beta})\\ &= \operatorname{argmin}_{\boldsymbol{\beta}}\left(\widehat{\boldsymbol{Q}}^{-1/2}\boldsymbol{w}-\widehat{\boldsymbol{Q}}^{-1/2}\boldsymbol{\Psi\beta}\right)^H\left(\widehat{\boldsymbol{Q}}^{-1/2}\boldsymbol{w}-\widehat{\boldsymbol{Q}}^{-1/2}\boldsymbol{\Psi\beta}\right)\\ &= (\boldsymbol{G}^H\boldsymbol{G})^{-1}\boldsymbol{Gv},\end{aligned} \tag{B.10}$$

where $\boldsymbol{G}=\widehat{\boldsymbol{Q}}^{-1/2}\boldsymbol{\Psi}$ and $\boldsymbol{v}=\widehat{\boldsymbol{Q}}^{-1/2}\boldsymbol{w}$. The expression (B.10) applies under hypothesis H_Θ, and the same expression with $\boldsymbol{\beta}=\mathbf{0}$ applies under hypothesis H_0.

With the above ML expressions for $\boldsymbol{Q}$, σ^2, and $\boldsymbol{\beta}$ under each hypothesis, the likelihoods are $\widehat{f}_\Theta(\boldsymbol{w},\boldsymbol{z})$ and $\widehat{f}_0(\boldsymbol{w},\boldsymbol{z})$, respectively, and their ratio is

$$\begin{aligned}\lambda &= \frac{\widehat{f}_\Theta(\boldsymbol{w},\boldsymbol{Z})}{\widehat{f}_0(\boldsymbol{w},\boldsymbol{Z})} = \left(\frac{\widehat{\sigma}^2_\Theta}{\widehat{\sigma}^2_0}\right)^{KR} = \left(\frac{\boldsymbol{w}^H\widehat{\boldsymbol{Q}}^{-1}\boldsymbol{w}}{(\boldsymbol{w}-\boldsymbol{\Psi}\widehat{\boldsymbol{\beta}})^H\widehat{\boldsymbol{Q}}^{-1}(\boldsymbol{w}-\boldsymbol{\Psi}\widehat{\boldsymbol{\beta}})}\right)^{KR}\\ &= \left(\frac{\boldsymbol{v}^H\boldsymbol{v}}{\boldsymbol{v}^H(\mathbf{I}-\boldsymbol{P_G})\boldsymbol{v}}\right)^{KR} = \frac{1}{\left(1-\frac{\boldsymbol{v}^H\boldsymbol{P_G}\boldsymbol{v}}{\boldsymbol{v}^H\boldsymbol{v}}\right)^{KR}} = \frac{1}{(1-\rho^2)^{KR}},\end{aligned} \tag{B.11}$$

where $\boldsymbol{G}=\widehat{\boldsymbol{Q}}^{-1/2}\boldsymbol{\Psi}$, $\boldsymbol{v}=\widehat{\boldsymbol{Q}}^{-1/2}\boldsymbol{w}$, $\boldsymbol{P_G}=\boldsymbol{G}(\boldsymbol{G}^H\boldsymbol{G})^{-1}\boldsymbol{G}$, and $\rho^2=\frac{\boldsymbol{v}^H\boldsymbol{P_G}\boldsymbol{v}}{\boldsymbol{v}^H\boldsymbol{v}}$. In the fourth equality, we have used the fact that $(\mathbf{I}-\boldsymbol{P_G})^2=\mathbf{I}-\boldsymbol{P_G}$.

A monotone function of λ is the coherence $\Lambda = 1-\frac{1}{\lambda^{1/(KR)}}=\rho^2$.

Acknowledgments. We are grateful to V. Chandrasekar for providing the CHILL data, and to Rob Beauchamp for help with its interpretation. We also thank Doug Cochran for many helpful discussions.

REFERENCES

[1] Y. I. Abramovich and O. Besson, *Fluctuating target detection in fluctuating k-distributed clutter*, IEEE Signal Process. Lett., 22 (2015), pp. 1791–1795.

[2] M. Bell and R. Grubbs, *JEM modeling and measurement for radar target identification*, IEEE Trans. Aerosp. Electron. Syst., 29 (1993), pp. 73–87.

[3] M. Butler and D. Johnson, *Feasibility of Mitigating the Effects of Wind Farms on Primary Radar*, Technical report W1400623, RenewableUK, London, United Kingdom, 2003.

[4] W.-S. Chen and I. S. Reed, *A new CFAR detection test for radar*, Digit. Signal Process., 1 (1991), pp. 198–214.

[5] E. Conte, M. Lops, and G. Ricci, *Asymptotically optimum radar detection in compound-Gaussian clutter*, IEEE Trans. Aerosp. Electron. Syst., 31 (1995), pp. 617–625.

[6] E. Conte, M. Lops, and G. Ricci, *Adaptive matched filter detection in spherically invariant noise*, IEEE Signal Process. Lett., 3 (1996), pp. 248–250.

[7] F. G. Friedlander, *Introduction to the Theory of Distributions*, Cambridge University Press, New York, 1982.

[8] B. Gallardo-Hernando, F. Perez-Martinez, and F. Aguado-Encabo, *Mitigation of wind turbine clutter in C-band weather radars for different rainfall rates*, in IEEE International Radar Conference, Piscataway, NJ, 2009, pp. 1–6.

[9] G. Greving, W.-D. Biermann, and R. Mundt, *Radar and wind turbines – RCS theory and results for objects on the ground and in finite distances*, in Microwaves, Radar and Remote Sensing Symp. (MRRS), IEEE, Piscataway, NJ, 2011, pp. 321–326.

[10] K. Hood, S. Torres, and R. Palmer, *Automatic detection of wind turbine clutter using Doppler spectral features*, in 34th International Conference on Radar Meteorology, Williamsburg, VA, American Meteorological Society, Boston, MA, 2009.

[11] K. Hood, S. Torres, and R. Palmer, *Automatic detection of wind turbine clutter for weather radars*, J. Atmos. Oceanic Technol., 27 (2010), pp. 1868–1880.

[12] B. M. Isom, R. D. Palmer, G. S. Secrest, R. D. Rhoton, D. Saxion, J. L. Winslow, J. Reed, T. Crum, and R. Vogt, *Characterization and mitigation of wind turbine clutter on the WSR-88D network*, in 33rd Conference on Radar Meteorology, 2007, Bureau of Meteorology, Melbourne, 8B8.

[13] B. M. Isom, R. D. Palmer, G. S. Secrest, R. D. Rhoton, D. Saxion, T. L. Allmon, J. Reed, T. Crum, and R. Vogt, *Detailed observations of wind turbine clutter with scanning weather radars*, J. Atmos. Oceanic Technol., 26 (2009), pp. 894–910, https://doi.org/10.1175/2008JTECHA1136.1.

[14] C. Jackson and M. Butler, *Options for mitigation of the effects of wind farms on radar sytems*, in International Conference on Radar Systems, IET, London, 2007, pp. 1–6.

[15] E. J. Kelly, *An adaptive detection algorithm*, IEEE Trans. Aerosp. Electron. Syst., AES-22 (1986), pp. 115–127.

[16] E. J. Kelly and K. M. Forsythe, *Adaptive Detection and Parameter Estimation for Multidimensional Signal Models*, Technical report 848, Lincoln Laboratory, Massachusetts Institute of Technology, Lexington, MA, 1989.

[17] S. Kraut and L. L. Scharf, *The CFAR adaptive subspace detector is a scale-invariant GLRT*, IEEE Trans. Signal Process., 47 (1999), pp. 2538–2541.

[18] S. Kraut, L. L. Scharf, and L. T. McWhorter, *Adaptive subspace detectors*, IEEE Trans. Signal Process., 49 (2001), pp. 1–16.

[19] S. Kraut, L. L. Scharf, and R. W. Butler, *The adaptive coherence estimator: A uniformly most-powerful-invariant adaptive detection statistic*, IEEE Trans. Signal Process., 53 (2005), pp. 427–438.

[20] F. Kong, *Wind turbine clutter mitigation for weather radar by adaptive spectrum processing*, in IEEE Radar Conference, IEEE, Piscataway, NJ, 2012, pp. 471–474.

[21] S. Manzato, B. Peeters, R. Osgood, and M. Luczak, *Wind turbine model validation by full-scale vibration test*, in Proceedings of the European Wind Energy Conference (EWEC), Vol. 11, Curran Associates, Red Hook, NY, 2010, pp. 395–409.

[22] W. Melvin and J. Guerci, *Knowledge-aided signal processing: A new paradigm for radar and other advanced sensors*, IEEE Trans. Aerosp. Electron. Syst., 42 (2006), pp. 983–996.

[23] J. J. McDonald, B. C. Brock, S. E. Allen, P. G. Clem, J. A. Paquette, W. E. Patitz, W. K. Miller, D. A. Calkins, and H. J. Loui, *Radar-cross-section reduction of wind turbines*, Technical report SAND2012-0480, Sandia, Albuquerque, NM, 2012.

[24] F. Nai, R. D. Palmer, and S. M. Torres, *Range-Doppler domain signal processing to mitigate wind turbine clutter*, in IEEE Radar Conference, 2011, pp. 841–845.

[25] A. Naqvi, S.-T. Yang, and H. Ling, *Investigation of Doppler features from wind turbine scattering*, IEEE Antennas Wireless Propag. Lett., 9 (2010), pp. 485–488.

[26] A. Naqvi and H. Ling, *Signal filtering technique to remove Doppler clutter caused by wind turbines*, Microw. Opt. Technol. Lett., 54 (2012), pp. 1455–1460, http://dx.doi.org/10.1002/mop.26819.

[27] P. Pakrooh, A. Homan, L. L. Scharf, M. Cheney, and M. Ferrara, *Multipulse adaptive coherence for detection in wind turbine clutter*, IEEE Trans. Aerosp. Electron. Syst., 53 (2017), pp. 3091–3103.

[28] R. Palmer, K. D. Le, and B. Isom, *Wind turbine clutter mitigation using fully adaptive arrays*, in European Radar Conference (EuRAD), IEEE, Piscataway, NJ, 2008, pp. 356–359.

[29] J. Perry and A. Biss, *Wind farm clutter mitigation in air surveillance radar*, IEEE Aerosp. Electron. Syst. Mag., 22 (2007), pp. 35–40.

[30] G. J. Poupart, *Wind farms impact on radar aviation interests–Final report*, Technical report, QinetiQ Ltd, Waltham, MA, 2003.

[31] F. C. Robey, D. R. Fuhrmann, E. J. Kelly, and R. Nitzberg, *A CFAR adaptive matched filter detector*, IEEE Trans. Aerosp. Electron. Syst., 28 (1992), pp. 208–216.

[32] M. Reed and B. Simon, *Methods of Modern Mathematical Physics. Vol.* 1 *Functional Analysis*, Academic Press, New York, 1972.

[33] L. L. Scharf, *Statistical Signal Processing: Detection, Estimation, and Time Series Analysis*, Addison-Wesley, New York, 1991.

[34] L. L. Scharf and L. T. McWhorter, *Adaptive matched subspace detectors and adaptive coherence estimators*, in Conference Record of the Thirtieth Asilomar Conference on Signals, Systems and Computers, IEEE Computer Society, Los Alamitos, CA, 1996, pp. 1114–1117.

[35] L. L. Scharf and B. Friedlander, *Matched subspace detectors*, IEEE Trans. Signal Process., 42 (1994), pp. 2146–2157.

[36] L. T. McWhorter, L. L. Scharf, and L. J. Griffiths, *Adaptive coherence estimation for radar signal processing*, in Conference Record of The Thirtieth Asilomar Conference on Signals, Systems and Computers, Vol. 1, IEEE Computer Society, Los Alamitos, CA, 1996, pp. 536–540.

[37] L. L. Scharf, P. Pakrooh, and R. W. Butler, *Coherence statistics for multipulse subspace detection*, IEEE Signal Process. Lett., 2018, submitted.

[38] P. J. Schubel and R. J. Crossley, *Wind turbine blade design*, Energies, 5 (2012), pp. 3425–3449, http://www.mdpi.com/1996-1073/5/9/3425.

[39] A. Shchuka and I. Sandhu, *Air Traffic Control Wind Turbine Interference Mitigation at Raytheon*, Raytheon, Waltham, MA, 2012.

[40] A. D. Siggia and R. E. Passarelli, *Gaussian model adaptive processing (GMAP) for improved ground clutter cancellation and moment calculation*, in Procedings of the 3rd European Conference on Radar Meteorology and Hydrology (ERAD), Copernicus GmbH, Berlin, 2004, pp. 67–73.

[41] B. Simon, *Quantum Mechanics for Hamiltonians Defined as Quadratic Forms*, Princeton University Press, Princeton, NJ, 1971.

[42] A. Sterns, L. Manuel, K. Saranyasoontorn, and L. Nelson, *Analysis of time series data on wind turbine loads*, Technical report, University of Texas, Austin, TX, 2003.

[43] P. Swerling, *Probability of Detection for Fluctuating Targets*, Technical report RM-1217, Rand Corporation, Santa Monica, CA, 1954, http://www.dtic.mil/dtic/tr/fulltext/u2/080638.pdf.

[44] F. Treves, *Basic Linear Partial Differential Equations*, Academic Press, New York, 1975.

[45] J. A. Trischman, S. Jones, R. Bloomfield, E. Nelson, and R. Dinger, *An X-band linear frequency modulated radar for dynamic aircraft measurement*, in AMTA Proceedings, Long Beach, CA, Springer, Berlin, p. 431.

[46] F. Uysal, U. Pillai, I. Selesnick, and B. Himed, *Signal decomposition for wind turbine clutter mitigation*, in Radar Conference, IEEE, Piscataway, NJ, 2014, pp. 60–63.

[47] N. Whitelonis, S.-T. Yang, and H. Ling, *Application of near-field to far-field transformation to Doppler features from wind turbine scattering*, IEEE Trans. Antennas Propag., 60 (2012), pp. 1660–1665.

[48] A. H. Zeemanian, *Distribution Theory and Transform Analysis*, Dover, New York, 1965.